Materials & Design 238 (2024) 112724

Contents lists available at ScienceDirect

Materials & Design

journal homepage: www.elsevier.com/locate/matdes

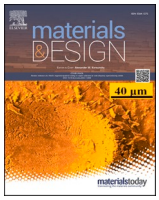

The impact of chemical short-range order on the thermophysical properties of medium- and high-entropy alloys

Angelo F. Andreoli [a,*], Andrea Fantin [b,c], Sergey Kasatikov [c], Vinícius P. Bacurau [a], Michael Widom [d], Piter Gargarella [a], Eric M. Mazzer [a], Thomas G. Woodcock [e], Kornelius Nielsch [e,f], Francisco G. Coury [a]

[a] Federal University of São Carlos, Department of Materials Engineering, Rodovia Washington Luís, km 235 SP-310, 13565-905 São Carlos, SP, Brazil
[b] Bundesanstalt für Materialforschung und -prüfung, Unter den Eichen 87, 12205 Berlin, Germany
[c] Helmholtz-Zentrum Berlin für Materialien und Energie GmbH, Hahn-Meitner Platz 1, 14109 Berlin, Germany
[d] Department of Physics, Carnegie Mellon University, 5000 Forbes Avenue, Pittsburgh 15213, USA
[e] IFW Dresden, Institute for Metallic Materials, Helmholtzstraße 20, 01069 Dresden, Germany
[f] Institute of Materials Science, Technische Universität Dresden, 01062 Dresden, Germany

ARTICLE INFO

Keywords:
High-entropy alloys
Chemical short-range order
Dilatometry
Differential scanning calorimetry
Order-disorder effects

ABSTRACT

The unusual behavior observed in the coefficient of thermal expansion and specific heat capacity of CrFeNi, CoCrNi, and CoCrFeNi medium/high-entropy alloys is commonly referred to as the K-state effect. It is shown to be independent of the Curie temperature, as demonstrated by temperature-dependent magnetic moment measurements. CoCrFeNi alloy is chosen for detailed characterization; potential reasons for the K-state effect such as texture, recrystallization, and second-phase precipitation are ruled out. An examination of the electronic structure indicates the formation of a pseudo-gap in the Density of States, which suggests a specific chemical interaction between Ni and Cr atoms upon alloying. Hybrid Monte Carlo/Molecular Dynamic (MC/MD) simulations indicate the presence of non-negligible chemical short-range order (CSRO). Local lattice distortions are shown to be negligible, although deviations around Cr and Ni elements from those expected in a fully disordered structure are experimentally observed by X-ray absorption spectroscopy. The determined bonding distances are in good agreement with MC/MD calculations. A mechanism is proposed to explain the anomalies and calorimetric experiments and their results are used to validate the mechanism.

1. Introduction

In 1951, German scientist Hans Thomas observed abnormal changes to the electrical resistivity, following heat treatments at low temperatures, for a series of metallic alloys including Ni-Cr, Fe-Al, Ni-Al, Ag-Mn, Ni-Cu, and Ni-Cu-Zn with neither apparent phase transformations nor magnetic transitions [1]. The phenomenon was described as the "*Komplex Zustand*," which translates to English as the 'complex state;' it is known today as the K-state effect. Later, it was demonstrated that this intriguing phenomenon affects not only the electrical resistivity but also other physical properties such as the coefficient of thermal expansion (CTE) [2], heat capacity (C_p) [3], thermal conductivity [4], and mechanical properties [5] of many alloys [6] containing at least one transition metal as the solvent element.

The occurrence of the K-state effect has been proposed to be related to (*I*) long-range atomic order (LRO) [5], observed after long-time annealing near the stoichiometric composition of intermetallic phases; (*II*) the formation of Guinier-Preston zones [7]; (*III*) chemical short-range order (CSRO) [8]; and (*IV*) changes in electronic configuration due to local lattice distortion (LLD) [9]. To date, the K-state effect is still not completely understood, with CSRO formation as the most accepted explanation, at least in single-phased face-centered cubic (*fcc*) alloys [6]. Ordering, be it short- or long-range, will result, according to Marucco and Nath, in [5]: (*i*) lattice parameter contraction, leading to dimensional instability; (*ii*) thermal and electrical characteristics variations; and (*iii*) changes in mechanical properties due to pile-ups of dislocation dipoles.

Short-range order appears to be more common in medium- (MEAs) and high-entropy alloys (HEAs) than assumed initially based on the entropic effect and has been the subject of theoretical and experimental

* Corresponding author.
E-mail address: angelo.andreoli@ufscar.br (A.F. Andreoli).

https://doi.org/10.1016/j.matdes.2024.112724
Received 23 November 2023; Received in revised form 6 January 2024; Accepted 29 January 2024
Available online 1 February 2024

investigations. The first theoretical study to report on CSRO in the CoCrNi MEA and the CoCrFeNi HEA was done by Tamm *et al.* [10]. The study used a hybrid computational method using Monte Carlo (MC) and molecular dynamics (MD) combined with Density Functional Theory (DFT) calculations. Simulated annealing at $T = 500$ K showed a significant degree of CSRO in CoCrNi, involving a 40 % reduction in the number of Cr-Cr pairs and an increase in the number of Ni-Cr and Co-Cr pairs. A comparable trend was reported for CoCrFeNi alloy with a substantial decrease in Cr-Cr and Fe-Fe pairs, a moderate decrease in Ni-Ni and Co-Co pairs, and an increase of Ni-Cr, Ni-Fe, and Cr-Co, and Co-Fe pairs. The reduction in the number of Cr-Cr pairs was correlated to the magnetic frustration resulting from Cr atoms being forced to align themselves ferromagnetically.

A reordering of Cr-Ni and Cr-Co pairs may cause the K-state effect on the heat capacity $c_p(T)$ as was proposed by Pei *et al.* [11] using the Wang-Landau MC method and simulated annealing algorithms in CoCrNi. These CSRO results agree with Tamm *et al.* [10] predictions and Zhang *et al.* X-ray and neutron scattering, and extended X-ray absorption fine structure (EXAFS) experiments [12]. Zhang *et al.* EXAFS results revealed that Cr is favorably bonded with Ni and Co, although the interpretation relied on DFT, showing how CoCrNi should not be considered a completely random solid solution despite not showing any long-range ordered phase.

Through energy-filtered transmission electron microscopy (TEM), Zhang *et al.* [13] suggested similar conclusions by observing noticeable streaks along the [1 1 1] directions between *fcc* Bragg spots and the dark field images from this region revealed nanoscale domains only in a CoCrNi annealed sample (1273 K, slow furnace cooling). On the other hand, Li *et al.* [14] recently proved that CSRO cannot be determined from TEM selected area electron diffraction (SAED) patterns, as the atomic scattering factors between Cr, Co, and Ni are practically equivalent. Furthermore, Coury *et al.* [15] showed that the fundamental origin of multiple diffuse intensities often ascribed to CSRO is indeed a universal phenomenon in all simple *fcc* materials.

Atom probe tomography was also employed for CSRO determination in the CoCrNi MEA by Inoue, Yoshida, and Tsuji [16] on annealed samples at 973 K for 384 h, after homogenization treatment, suggesting that Cr-rich {0 0 1} and (Ni + Co)-rich {0 0 1} atomic layers tended to align mutually. Particularly relevant is defining the specimen heat-treatment history as it was demonstrated to affect CSRO in CrCoNi by Du *et al.* [17]. They deduced from their time–temperature CSRO maps that in the water-quenched samples, CSRO was not well-developed but still present to a minor degree. On the contrary, more robust CSRO should be generated during the slow furnace process, especially at temperatures below 873 K. Moreover, during a reheating, simulations would indicate that at this temperature range (800 to 1000 K), a considerable amount of destruction of the CSRO should occur [17]. Depending on the heat-treatment history, CSRO maximum domain size was established to vary between less than 7 Å (*ca.* two unitary cells) at 1400 K to 19 Å for samples aged at 773 K for 10 h.

Even though all the above-mentioned theoretical and experimental studies reveal evidence of CSRO in different *fcc* based MEA/HEAs, a heated debate on whether CSRO influences the mechanical properties is still ongoing [13,18–20], as only a few experimental [14,21–23] or theoretical [10,11,17,24–27] reports discuss or propose causation between the two.

This study aims to tackle this specific question by investigating the thermophysical properties of the CoCrFeNi HEA and two MEAs – CrFeNi and CoCrNi – subsystems, suggesting if and how phase transformations, magnetic, microstructural, structural transitions and ultimately CSRO in terms of atomic and electronic rearrangements may be the ultimate cause of the K-state effect. Laboratory-based techniques (*e.g.*, dilatometry and calorimetry) and synchrotron-based techniques supported by MC/MD simulations will be used for this purpose, as the formers can detect order–disorder transitions due to lattice parameters and specific heat capacity $c_p(T)$ variations and the latter can reveal information on preferred atomic bonds and electronic band structure.

2. Materials and methods

Samples of CrFeNi, CoCrNi, and CoCrFeNi equiatomic alloys were prepared by vacuum arc melting from high-purity elements (≥99.99 %) and cast into a copper mold. Each sample was flipped and remelted at least four times before casting to ensure chemical homogeneity.

Thermal expansion measurements were carried out using a Netzsch DIL 402C dilatometer from 400 to 1263 K at a heating–cooling rate of 10K • min^{-1}. The measurements were done on 25 mm long rods under an Ar atmosphere using a sample holder and a pushrod made of fused silica. The equipment was calibrated using fused silica standard specimens from Netzsch. The analysis of the measured data was performed using the Netzsch Proteus® software.

The temperature-dependent magnetic moment was measured on 1 mm in length and 4.5 mm in diameter samples. The heating–cooling cycles at 5 K • min^{-1} were carried out in the temperature range of 10–900 K. The measurements were performed separately in 10–350 K and 300–900 K temperature ranges. The applied magnetic field was equal to 1000 Oe using the Vibrating Sample Magnetometer option of a Quantum Design Physical Property Measurement System.

The c_p was measured by differential scanning calorimetry (DSC). The measurements were carried out on ~40 mg specimens under an Ar-flow with a Netzsch-DSC404C device at a heating and cooling rate of 10 K • min^{-1}. The heating–cooling cycles were repeated twice to eliminate the effect of exothermic reactions due to non-equilibrium cooling during casting [22]. An empty Al_2O_3 or platinum (increased sensibility) crucible was measured as a reference baseline, and sapphire was used as reference material [28]. Table S1 in the Supplementary Materials (S.M.) displays the heating–cooling programs. The c_p was calculated using the Netzsch Proteus® software according to the method described in Ref. [28].

Rod-like samples of the alloys were thermally treated under a constant Ar flow to investigate the microstructure and phase transformations upon aging, annealing, and/or homogenization (Table 1). The microstructure and phase constitution of the samples were analyzed using a scanning electron microscope (SEM) equipped with an electron-backscattered diffraction (EBSD) detector. Laboratory X-ray diffraction (Lab-XRD, Co-anode, current: 40 mA, voltage: 40 kV, Q-range: 2–6 $Å^{-1}$) was used to determine the phase constitution of as-cast and heat-treated samples. The diffraction patterns were analyzed using the X'Pert HighScore Plus software [29].

Annealed and aged samples were furnace-cooled, H – H-homogenized (water quenched). XRD – high-energy synchrotron XRD. Lab-XRD – laboratory XRD. MC/MD simulations were performed on the CoCrFeNi homogenized and quenched condition.

The CoCrFeNi alloy (as-cast and heat treated, see Table 1), 4.5 mm in diameter and 1 mm in length samples) was further investigated using high-energy synchrotron XRD at the beamline P21.1 (PETRA III, DESY Hamburg). The energy of photons and the beam size were 101.55 keV and 1 × 1 mm^2, respectively. Two-dimensional (2D) XRD patterns were taken by a hybrid pixel PILATUS3 X 2 M CdTe detector (DECTRIS). Using the FIT2D software [27], the recorded 2D images were azimuthally integrated to obtain XRD intensities as functions of the diffraction vector $Q = \frac{4\pi\sin\theta}{\lambda}$, where θ is the diffraction angle, and λ is the wavelength.

Samples for TEM were prepared by grinding the alloys down to a 50-μm thickness, and the final thinning was performed by argon ion milling on Gatan PIPS equipment. The samples were analyzed by TEM on a FEI FEG Tecnai (G20 model) operating at 200 kV.

EXAFS was conducted at the beamline KMC-3 [30,31] at the synchrotron light source BESSY II of Helmholtz-Zentrum Berlin. Spectra were collected at room temperature for Cr, Fe, Co, and Ni K-edges with a fixed k step of 0.05 $Å^{-1}$ up to a $k_{max} = 14$ $Å^{-1}$ (Cr, Ni) and a $k_{max} = 12.4$

Table 1
Details on the thermal history of the samples investigated and the characterization tools used for analyzing the structural and microstructural features of CrFeNi, CoCrNi, and CoCrFeNi alloys.

Condition	Alloy	Temperature (K)	Time (h)	Characterization methods
As-cast	CrFeNi	———	———	Lab-XRD, SEM
	CoCrNi			Lab-XRD, SEM
	CoCrFeNi			Lab-XRD, SEM, XRD, EXAFS
H + Aged	CoCrFeNi	773	10	TEM, XRD
H + Annealed	CrFeNi	973	24	Lab-XRD, SEM
	CoCrNi			Lab-XRD, SEM
	CoCrFeNi			Lab-XRD, SEM, XRD, EXAFS, NEXAFS, XPS
H + quenched	CrFeNi	1473	2	Lab-XRD, SEM
	CoCrNi			Lab-XRD, SEM
	CoCrFeNi			Lab-XRD, SEM, XRD, TEM, EXAFS, NEXAFS, XPS

$Å^{-1}$ (Fe, Co). Fe and Co K-edges signals suffer from intrinsic range limitations due to the alloy's neighboring Z + 1 elements (Z: atomic number). EXAFS data were collected in fluorescence mode with a 13-element energy-resolving silicon-drift detector. Pure metal reference foils (5–7 μm thickness) of Cr, Fe, Co, and Ni were measured in transmission mode up to $k_{max} = 16$ $Å^{-1}$ for energy calibration purposes.

First principles hybrid Monte Carlo/molecular dynamics (MC/MD) runs [32] were performed at 1473 K (homogenization temperature) on a 256-atom 4 × 4 × 4 *fcc* supercell using the equiatomic CoCrFeNi composition and a lattice parameter of 3.652 Å, extrapolated from the thermal expansion. Spin-polarized DFT calculations utilized the Vienna Ab initio Simulation Package code [33] with projector-augmented wave potentials [34] in the Perdew-Burke-Ernzerhof generalized gradient approximation [35]. DFT calculations used a single electronic *k*-point and a default cutoff energy of 269.532 eV, which is the highest default cutoff for this alloy system.

The simulations alternated 20 fs of molecular dynamics with five attempted Monte Carlo swaps. The average swap rate among Fe, Co, and Ni was 54 %, while swaps involving Cr averaged 22 % acceptance. After preliminary equilibration of six independent initial structures each for over 1000 attempted MC swaps and 4000 fs of molecular dynamics, the data collection run extended an additional 175 attempted MC swaps and 700 fs of molecular dynamics. Warren-Cowley order parameters [36,37] were defined as:

$$W_{ij} = 1 - \frac{P_{ij}}{x_i x_j},$$

where P_{ij} is the probability that the nearest neighbor pair joins species *i* and *j*, and $x_i = x_j = 1/4$ are the concentrations of species *i* and *j*. Each of the final independent structures were selected for conventional MD runs of 600 fs at 300 K using the experimentally observed lattice constant (3.572 Å). Peak positions and heights' uncertainties are standard deviations across the six independent runs.

Near-edge X-ray absorption fine structure (NEXAFS) spectroscopy and X-ray photoelectron spectroscopy (XPS) measurements of CoCrFeNi and reference pure elements (Cr, Co, Fe, and Ni) were performed at the RGL-PES station of the Russian-German beamline (RGBL) at the synchrotron light source BESSY II of Helmholtz-Zentrum Berlin. Before the NEXAFS and XPS measurements, the surface of each specimen was cleaned from oxides *in situ* under ultra-high vacuum conditions via diamond needle file scratching. The reference pure metals were heat-treated *in situ* for 20 min at 973 K to achieve higher surface purity. The NEXAFS and XPS spectra were measured at an incident photon angle of 55° with an energy resolution better than $E/\Delta E = 2000$. To ascertain the bulk-surface signal homogeneity, the NEXAFS spectra were obtained in two acquisition modes: total electron yield (TEY) and fluorescence yield (FY). The absolute photon energy scale was calibrated by measuring a gold single crystal's Au $4f_{7/2}$ photoelectron line (84.0 eV). Besides, the binding energy scale of XPS spectra was corrected by a Valence Band (VB) spectrum inflection point (Fermi level position) alignment to 0 for each specimen.

3. Results

3.1. Thermophysical properties

The temperature dependences of the CTE of the three alloys, measured during the first heating in the as-cast condition, are shown in Fig. 1a. The thermal expansion curves are shown in Fig. S1 in the S.M. In the low-temperature range (below ~800 K), CoCrNi shows a slightly lower CTE than CrFeNi and CoCrFeNi compositions. All three alloys have remarkably similar CTE in the high-temperature limit (above ~900 K). The values of CTE extracted from the dilatometry curves are 22.27, 22.77, and 22.04 (10^{-6} K^{-1}) for CrFeNi, CoCrNi, and CoCrFeNi at 1260 K, the highest experimental temperature. A valley in the temperature dependencies of CTE is seen for all three alloys in the range of ~750–950 K (Fig. 1a).

Two heating cycles were conducted to understand if the discontinuities observed on the first heating (Fig. 1a) were reversible. After the first cycle, the surface of the samples was ground (600 mesh sandpaper) and cleaned in an ultrasonic bath with isopropanol. The cycles for the CoCrFeNi HEA are shown in Fig. 1b. As observed, in the first heating, a minimum occurs at ~850 K, followed by an increase in the CTE with rising temperature. However, the second heating cycle has no minimum on the CTE(*T*) curve. Instead, a sudden rise in CTE occurs at the same temperature range where the minimum in the first heating is observed (Fig. 1b). The CTE varies quasi-linearly below (~800 K) and above (~920 K) the valley. However, the slopes are different, indicating that a magnetic transition, a first- or second-order phase transformation, or a microstructural transition in the alloys may exist. It is observed that the phenomenon is reversible by comparing the first and second heating cycles (Fig. 1b). Thus, it cannot be attributed to quenched-in vacancies and phenomena of recrystallization or any stress relief from solidification.

A comparison of the CTE at 700 K in this work and Refs. [38,39] (limited to 700 K) is shown in Table 2. One may note an excellent agreement with the values described here and for polycrystalline CoCrNi and CoCrFeNi alloys reported in Ref. [38]. For the CrFeNi alloy, there is a slight difference observed.

In Fig. 2, the temperature-dependent magnetic moment of the three alloys is presented. No magnetic transition is observed for all alloys in the 293 to 1073 K temperature range. The determined Curie temperatures T_c are, respectively, 23 and 134 K for CrFeNi and CoCrFeNi. It was not possible to determine the T_c of the CoCrNi alloy since it is below the

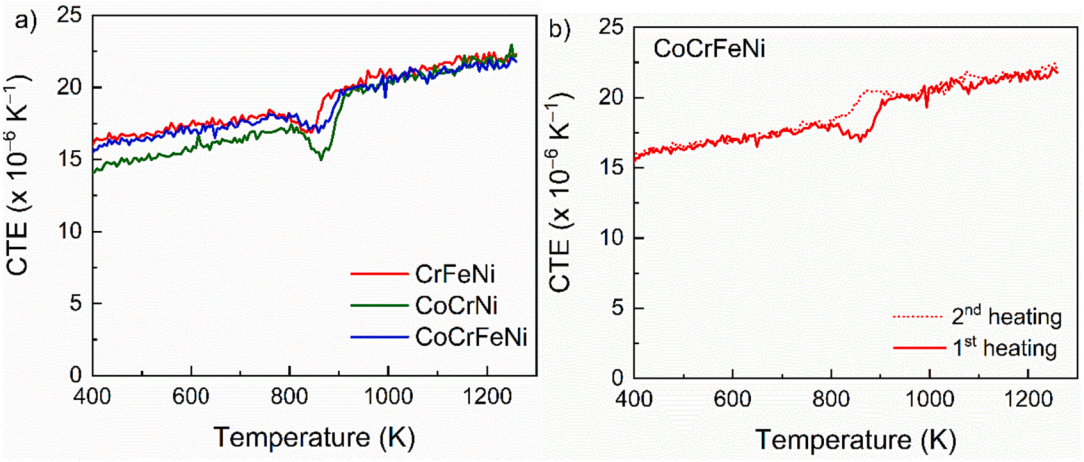

Fig. 1. (a) The coefficient of thermal expansion CTE of CrFeNi, CoCrNi, and CoCrFeNi alloys measured during the first heating (10 K • min^{-1}); (b) CTE of the CoCrFeNi alloy measured during the first and second heating cycles.

Table 2
Comparison of the coefficient of thermal expansion CTE between this study and those reported in the literature.

Alloy	CTE at 700 K (10^{-6} K^{-1})		
	Ref. [39]	Ref. [38]	This study
CrFeNi	–	16.6	17.8
CoCrNi	–	16.4	16.5
CoCrNi*	16.0	–	–
CoCrFeNi	–	17.3	17.4

* Single-crystal.

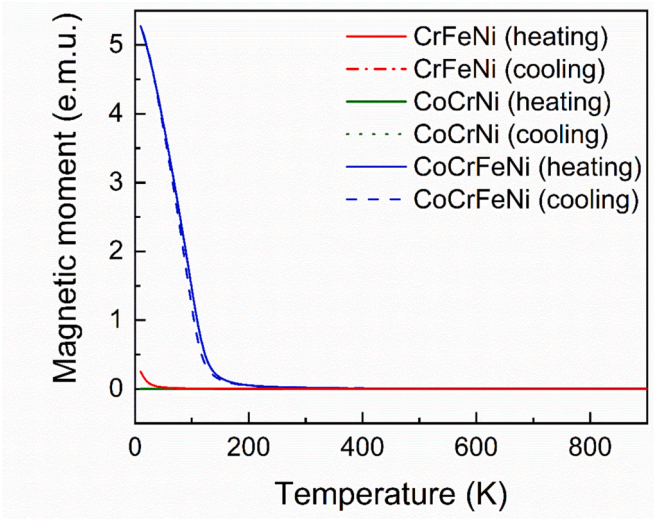

Fig. 2. The temperature-dependent magnetic moment during a heating–cooling cycle (5 K • min^{-1}) of CrFeNi, CoCrNi, and CoCrFeNi alloys. The curves overlap over almost all temperature ranges.

low limit of 10 K in the experimental setup. Literature reports the value of 7 K [40].

The specific heat capacity c_p of the CrFeNi, CoCrNi, and CoCrFeNi alloys as a function of temperature (400–973 K) is shown in Fig. 3. Again, in the first heating, all three alloys show minima in the $c_p(T)$ curves (exothermic reaction) in the temperature range of 730–950 K, followed by a steep increase in the $c_p(T)$ (endothermic reaction) upon further heating. One may note that during the second heating, all alloys show a steep increase in c_p in the same temperature range as the first heating. However, no minima occur. As the samples were heated and cooled for two consecutive cycles, it confirms that the phenomenon is reversible. These temperatures match the observed transition on the CTE curve. Furthermore, the fact that these temperatures are very different from the T_c, shown in Fig. 2, further reinforces their non-magnetic nature.

3.2. Structural and microstructural characterization

Fig. 4a displays the room temperature lab-XRD profiles of the as-cast and annealed (973 K for 24 h) CrFeNi, CoCrNi, and CoCrFeNi alloys. In both conditions, only Bragg peaks corresponding to an *fcc* structure are distinguishable for all alloys. The changes in the peak intensity ratio are likely due to the large grain size of the samples, leading to inherently poor grain statistics. Nonetheless, to confirm that no texture changes occurred upon annealing, samples were further investigated by EBSD, as shown later.

The corresponding microstructures are shown in Fig. 4b. The SEM images of the CoCrNi and CoCrFeNi samples exhibit a single-phase solid solution (SPSS) in both conditions. In contrast to the XRD profile shown in Fig. 4a, the SEM images of the annealed CrFeNi alloy reveal precipitates of a minor second phase at the grain boundaries (Fig. 4b), which could not be detected by XRD. They are indicating that such a second phase would correspond to a low volume fraction. The observed second-phase precipitation in the CrFeNi alloy could explain the anomaly observed in the thermophysical properties (Fig. 1a and 3). Therefore, no further characterizations and investigations were carried out on this alloy. The formation of precipitates at the grain boundaries of the CrFeNi alloy after thermo-mechanical processing and annealing has been reported by Laplanche *et al.* [38]. Based on XRD and EBSD data, they determined that the precipitates had a body-centered cubic (*bcc*) structure. CALPHAD predicts precipitation of a *bcc* phase in the CrFeNi equiatomic composition below 1273 K; see Fig. S2 in the S.M.

It is known that SEM and lab-XRD have limited spatial and volume fraction resolution for detecting second-phase precipitates. To gain a deeper understanding of the effects of structural and microstructural changes that could occur during the thermophysical measurements, the CoCrFeNi alloy was chosen for further investigations. Second-phase precipitation, crystallographic texture, recrystallization, and atomic and electronic structure were studied using synchrotron XRD, TEM, EBSD, EXAFS, NEXAFS, and XPS (Table 1). The homogenized and quenched CoCrFeNi was also investigated by MC/MD simulations. The CoCrFeNi alloy was chosen because it was shown to remain a SPSS after heat treatment (Fig. 4), while the CoCrNi MEA has already been extensively investigated.

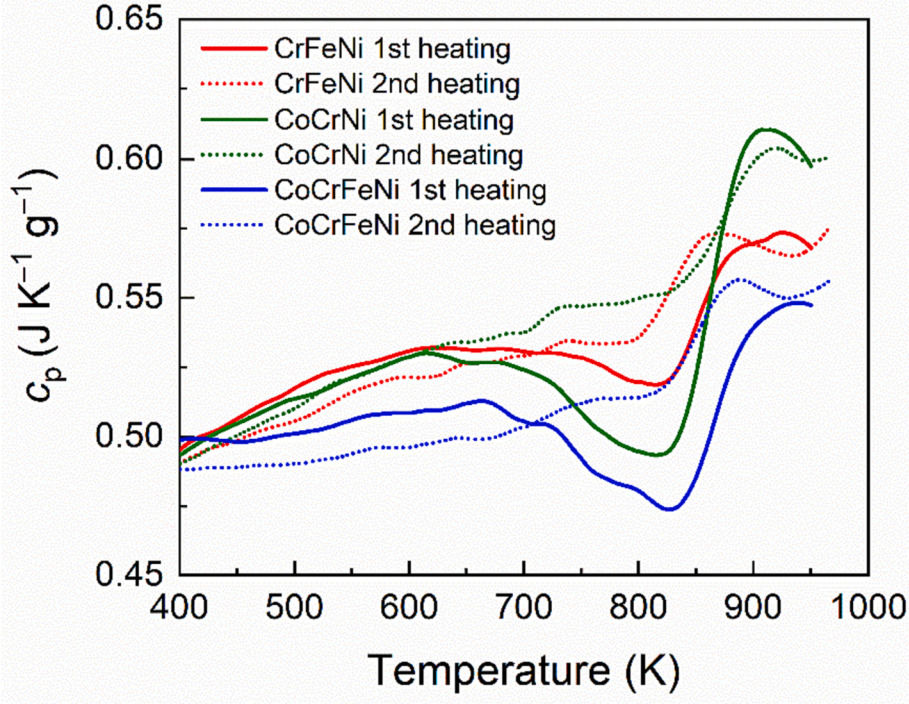

Fig. 3. The specific heat capacity c_p of CrFeNi, CoCrNi, and CoCrFeNi alloys measured during the first and second heating at a rate of.10 K • min^{-1}.

The synchrotron XRD patterns for as-cast and heat-treated samples of the CoCrFeNi alloy are shown in Fig. 5. The intensities of the two measurements were normalized to exclude any influence of sample dimensions. Corroborating the XRD results shown in Fig. 4, only an *fcc* SPSS is observed for all conditions; no other diffraction peaks are seen. A difference in the intensity of similar peaks, e.g. (1 1 1), is observed. It is essential to mention that the X-ray spot size is small, and possibly only a few grains were illuminated by the electromagnetic beam, which could explain the observed difference in the reflection intensities. The lattice parameters, derived from the XRD data for specimens with different thermal histories, are given in Table 3. The ± sign denotes the 1σ standard error.

EBSD maps were obtained from an as-cast sample and after the two-cycle dilatometry measurements of the CoCrFeNi HEA. Fig. 6 shows the grain map distributions, phase maps, and inverse pole figures (IPF) in the longitudinal direction. The most noticeable feature is that grain growth occurred during the dilatometry measurement. Grain growth can be visually observed by comparing the grain sizes of the as-cast and dilatometry samples from the grain maps. The grains are aligned in the longitudinal direction in the dilatometry sample, revealing a more regular morphology than those from the as-cast sample.

In Fig. 7, the TEM results are presented for selected samples homogenized at 1473 K for 24 h (water quenched) and a second sample that was subsequently aged for 10 h at 773 K, followed by slow furnace cooling. The TEM analysis reveals single-phase microstructures, as shown by the energy-dispersive X-ray spectroscopy (EDS) compositional maps in Fig. 7b-e. The [1 1 1] and [1 1 2] selected area diffraction patterns (SADPs) are displayed in Fig. 7g-h for both conditions. It is noteworthy that no additional superlattice reflections are observed, and the weak intensities observed at the $^1/_3${4 2 2} and ½{3 1 1} directions in the [1 1 1] and [1 1 2] SADPs, respectively, are also present in both conditions. The origin of these reflections was recently explained by Coury et al. as a universal phenomenon of simple *fcc* crystals [15]. It indicates that their nature did not change with the annealing for 10 h at 773 K. These results prove that the anomalous effects observed in the physical properties measurements are not due to the precipitation of any nanometric second phase.

3.3. Monte Carlo/molecular dynamics simulations

Simulations on CoCrFeNi were performed to combine predicted results on bond lengths with EXAFS experimentally determined ones. MC/MD can determine preferred pairs at the homogenization temperature. The results of $g(r)$ as a function of the distance are reported visually in Fig. S10 in the S.M. The atomic pair distances and the corresponding pair frequency data are resumed in Table 4.

Table 4 reveals that smaller atoms (Ni, Co) prefer to bond with atoms with a larger atomic radius, such as Cr and Fe, and vice versa, while the same element pairs are disfavored. It can also be noticed that at the temperature at which the Warren Cowley parameters were extracted (1473 K), only slight deviations from the complete disorder are present, as expected, with WC values oscillating between − 0.10 and + 0.20. The most favored pair is the Cr-Ni pair, followed by Cr-Co and Ni-Fe. On the other hand, Cr-Cr, Ni-Ni, and Fe-Fe are the most unfavored pairs.

3.4. X-ray absorption spectroscopy

A binary model was employed to fit the CoCrFeNi EXAFS data where scattering paths were modeled on *absorbing atom–grey metal (M)* bonds, with *M* assumed to be Fe (Z_{avg} = 26.25). Details are resumed in the S.M. with similar modeling and analyses published elsewhere [41]. No difference neither in EXAFS spectra (k-space, Fig. S3 in S.M.) nor in refined bond lengths between the as-cast, homogenized, and annealed specimens is observed within the accuracy of the technique (see Fig. S4 in the S.M.), generally agreed to be around 0.01–0.02 Å [42], and often reported to be 0.01 Å in several EXAFS works on MEA and HEAs [43].

Table 5 displays the relevant results obtained for the homogenized specimen – assumed to be representative of the three conditions. All fits' details, including pure metallic references and alloys' refined values, are reported in the S.M.

Notice that from EXAFS refinements carried out on pure Co and Ni metals, Co and Ni extracted metallic radii (*i.e.*, half the 1st shell distances) are within 0.005 Å of the tabulated ones. Therefore, in the negligibly distorted CoCrFeNi alloy, 0.01 Å can be assumed as a reasonable estimated accuracy value at any edge. Figures, including

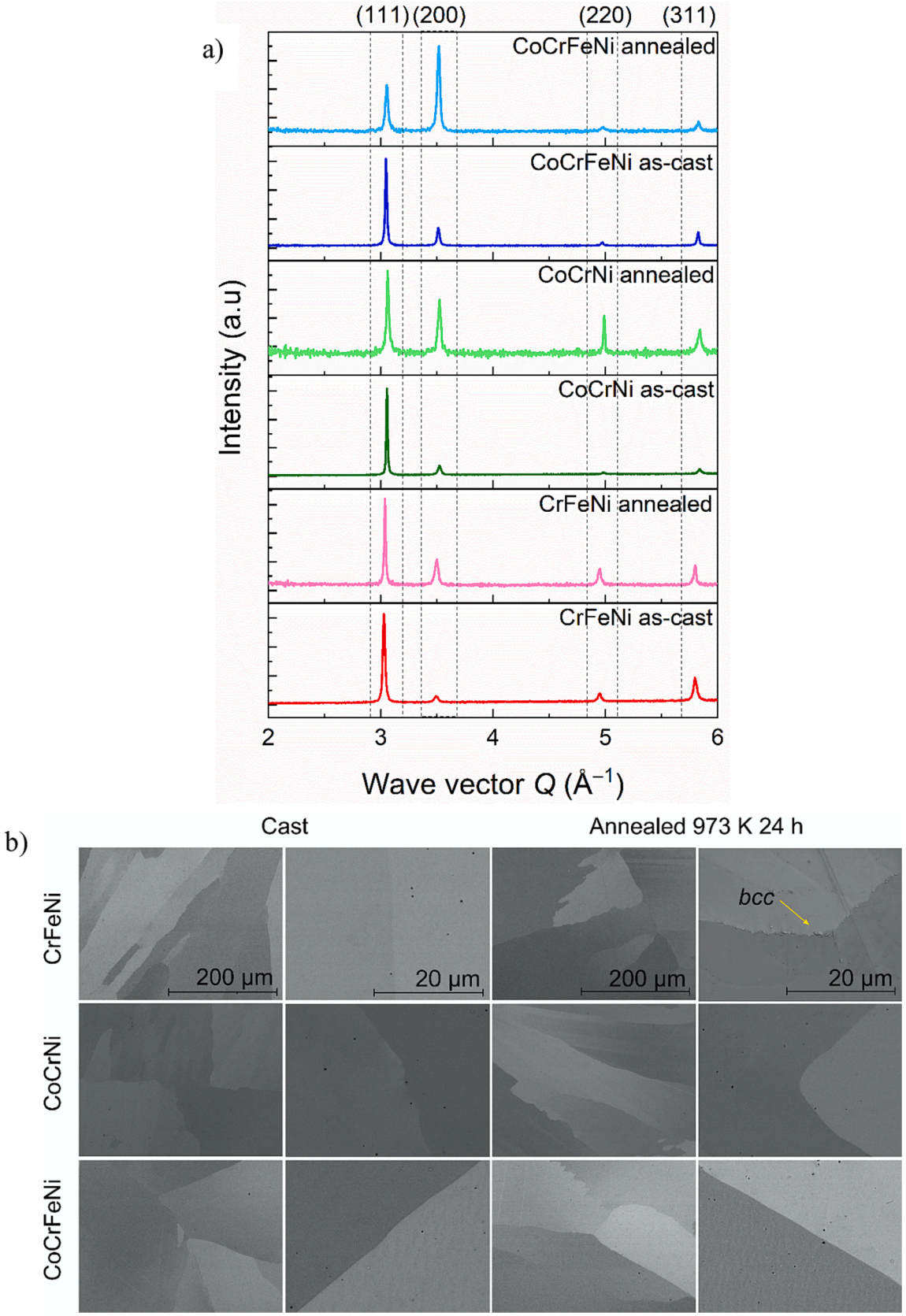

Fig. 4. (a) In the as-cast and annealed conditions, laboratory X-ray diffraction patterns of CrFeNi, CoCrNi, and CoCrFeNi alloys. (b) The microstructures of CrFeNi, CoCrNi, and CoCrFeNi alloys at two different magnifications: as-cast (two first columns) and annealed condition (two last columns).

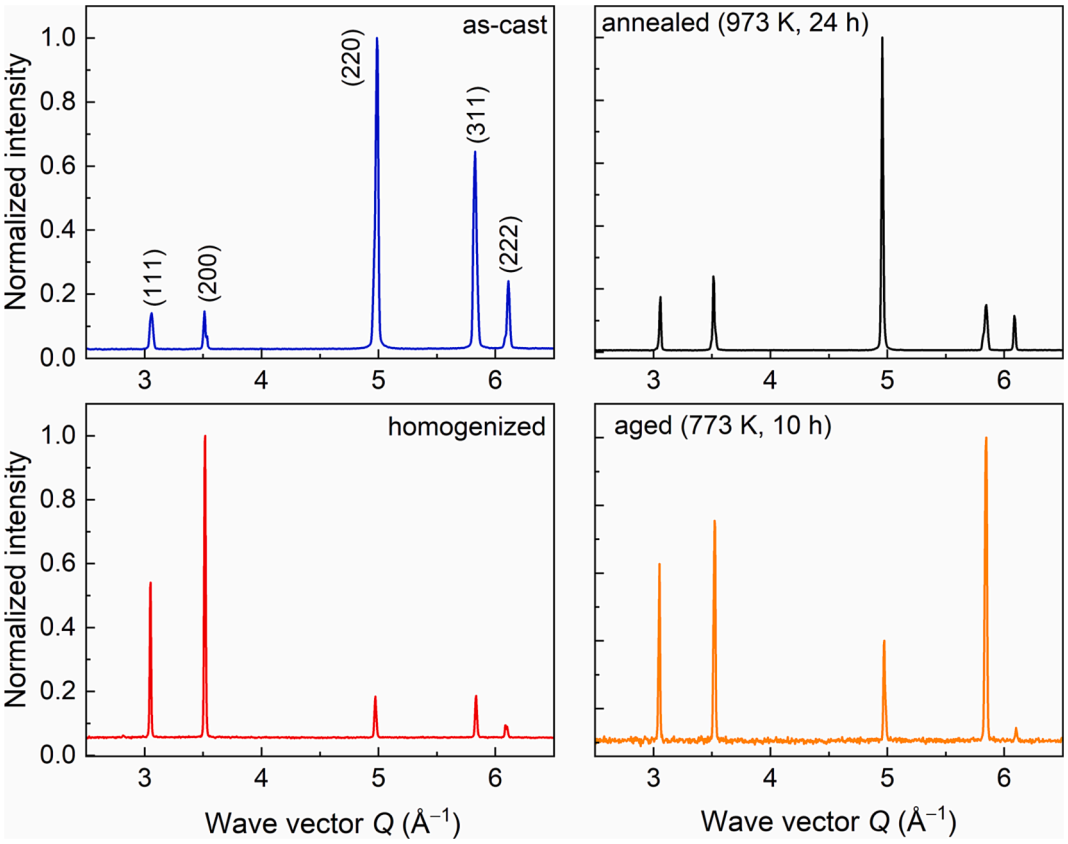

Fig. 5. Synchrotron XRD patterns comparing the CoCrFeNi HEAs' crystal structures with different thermal histories. The aged and annealed samples were previously homogenized at 1473 K for 2 h and water-quenched.

Table 3
Determined lattice parameters for the CoCrFeNi HEA with different thermal histories.

Sample	Lattice parameter (Å)
As-cast	3.568 ± 0.005
Aged (773 K, 10 h)	3.569 ± 0.006
Annealed (973 K, 24 h)	3.571 ± 0.007
Homogenized	3.572 ± 0.005

EXAFS results, will use 0.01 Å uncertainty (*ca.* 3σ and EXAFS accuracy), allowing for absolute length comparison with, *e.g.*, diffraction. However, only refinement uncertainties (*i.e.*, 1σ) will be presented in all reported EXAFS data tables.

The 1st shell results are compared in the following plot (Fig. 8) with the expected values from metallic radii, assuming no CSRO is present. The average distortion of local structure is ~−0.2(2) % at the 1st shell, negligible within the uncertainties, and compatible with results reported by PDF on the same nominal composition [44,45]. Authors report negligible distortions in CoCrFeNi alloy, both experimentally [12,44,46]

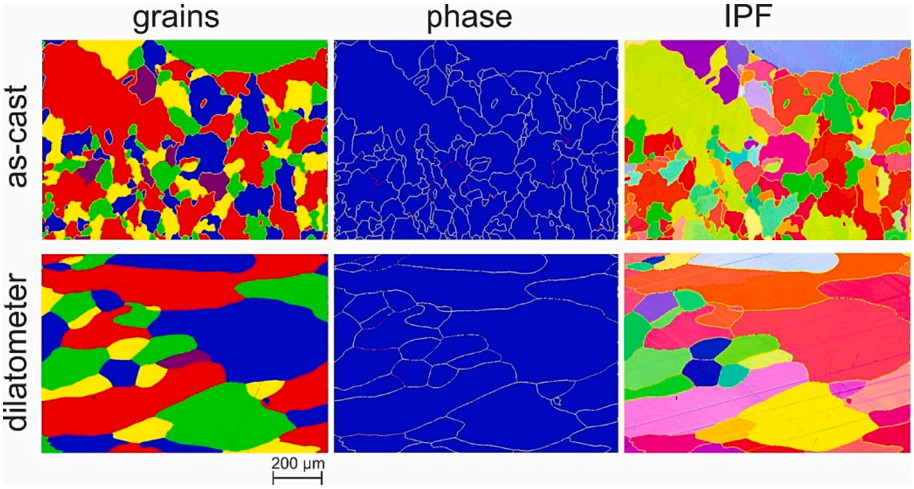

Fig. 6. EBSD maps of the CoCrFeNi HEA in the as-cast condition (1st row) and after the dilatometry measurement (2nd row). Left panels – grain maps; central panels – phase maps; right panels – inverse pole figures.

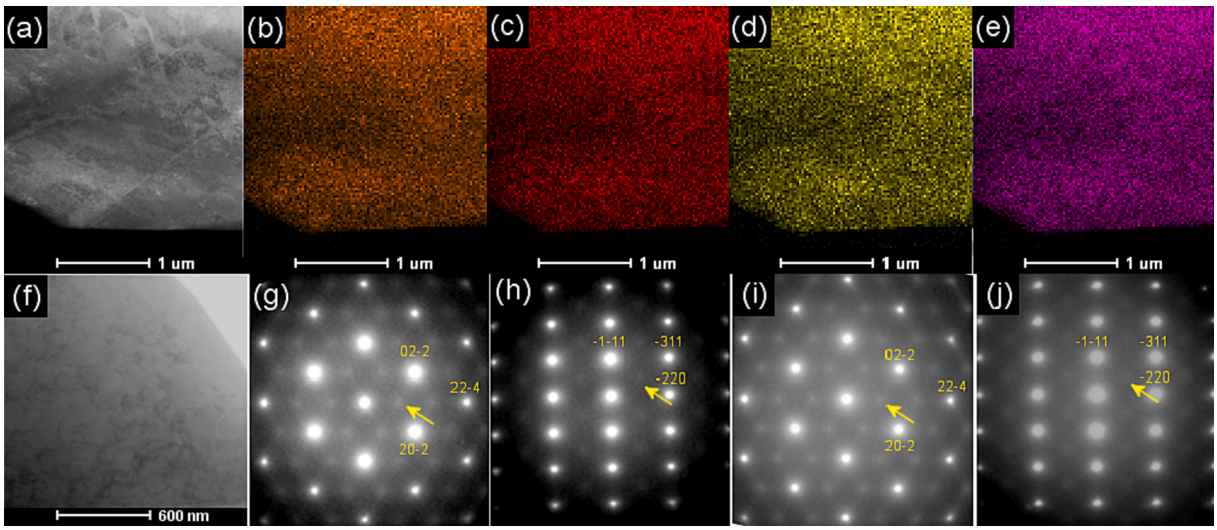

Fig. 7. Transmission electron microscopy analysis of the CoCrFeNi HEA in the aged condition via STEM-HAADF analysis (a) and EDS compositional mapping of (b) Cr, (c) Co, (d) Ni, and (e) Fe. On (f) the STEM-BF image of the same sample on the aged condition is shown. No precipitates are visible in either condition. The [1 1 1] and [1 1 2] SADPs of the alloys on the aged (g,h) and homogenized (i,j) are also shown, respectively. The intensity of all the SADPs is displayed on a logarithmic scale to enhance the visibility of fine details. No sharp additional superlattice reflections are seen in either pattern. The arrows indicate the diffuse extra in intensities at the $^1/_3\{4\,2\,2\}$ and $½\{3\,1\,1\}$ positions.

Table 4
The interatomic distances and the Warren Cowley parameters for each atomic pair in the homogenized (1473 K) and quenched CoCrFeNi HEA were determined by MC/MD simulations, ordered by favored to disfavored from top to bottom.

Pair	Interatomic distance (Å)	Warren Cowley parameters
Cr-Ni	2.523(5)	−0.10(3)
Cr-Co	2.505(5)	−0.07(2)
Fe-Ni	2.518(4)	−0.07(5)
Fe-Co	2.512(4)	−0.01(4)
Cr-Fe	2.520(6)	0.00(3)
Co-Co	2.507(5)	0.04(5)
Co-Ni	2.520(5)	0.07(4)
Fe-Fe	2.540(8)	0.11(7)
Ni-Ni	2.513(7)	0.12(7)
Cr-Cr	2.55(3)	0.20(5)

Table 5
EXAFS refinements' results (uncertainty: 1σ) on the homogenized CoCrFeNi for each measured edge (Cr, Fe, Co, and Ni), from left to right: amplitude factor S_0^2, 1st to 4th shell distances, Debye Temperature, and R-factors. XRD extrapolated distances from synchrotron X-ray diffraction are reported for comparison in the last row.

Edge	S_0^2	d 1st (Å)	d 2nd (Å)	d 3rd (Å)	d 4th (Å)	Θ_D (K)	R-factor (%)
†Cr K	ǂ0.63	2.527 (4)	3.57(2)	4.395 (6)	5.07(1)	367 (11)	1.0
†Fe K	ǂ0.61	2.520 (3)	3.56(1)	4.385 (6)	5.063 (7)	405 (10)	0.5
Co K	ǂ0.60	2.514 (3)	3.58(1)	4.387 (7)	5.064 (7)	374 (8)	0.5
Ni K	ǂ0.60	2.520 (3)	3.59(1)	4.383 (7)	5.057 (7)	401 (11)	0.7
XRD		2.526 (4)	3.572 (5)	4.375 (6)	5.052 (7)		

ǂ Parameter fixed to the correspondent reference foil.
† Corrected by Self Absorption (ATHENA, Fluo algorithm).

and by calculations [47]. Though 1st shell distortions of −0.2(2) % may still be relevant as the EXAFS technique reveals more information and is more accurate than PDF on the local scale, one can notice that already at

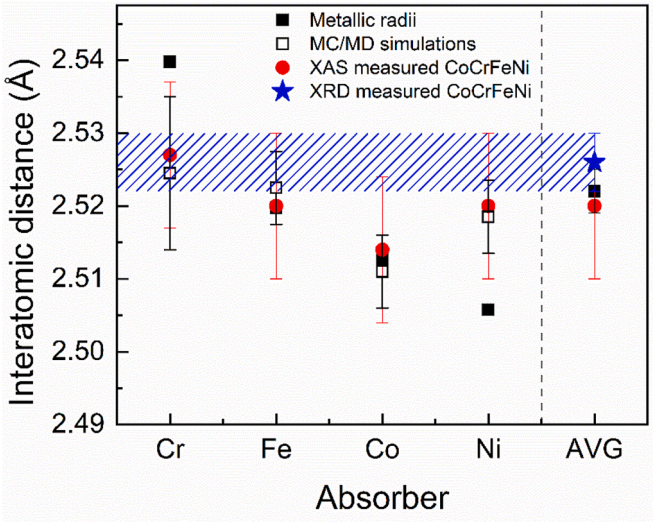

Fig. 8. Comparison of 1st shell bond length distances determined from EXAFS (red markers), XRD data (blue dashed region), and tabulated metallic radii, assuming a hard-sphere model and MC/MD simulations. (For interpretation of the references to color in this figure legend, the reader is referred to the web version of this article.)

the second shell level (Table 5), such distortions are within the unit cell size found by XRD, *i.e.*, ~0.0(4) %. Thus, an agreement with the statements on *fcc*-based HEAs not presenting distortions above the 1st shell level [48] is found.

Suggestions on the atomic radii of 3*d* transition metals are reported in different studies, depending on the atomic surrounding of each element, as well as for a CoCrFeNi specimen [45]. Cr, Fe, Co, and Ni radii are reported to be 1.23, 1.22, 1.23, and 1.23 Å, respectively, contrarily to the tabulated radii in pure metals of 1.280 Å [49], 1.260 Å [50], 1.253 Å [51] and 1.246 Å [52]. Assuming the simulated values are correct, bond lengths retrieved by EXAFS would fall several hundredths of Å short. Instead, suppose that an average atomic size in CoCrFeNi from the XRD lattice parameter $a = 3.572(5)$ Å could be extracted. From the 1st shell distance of 2.526(4) Å (*cf.* Table 5), assuming a hard spheres

model, R_{avg} = 1.263(2) Å, also assuming that no distortions and no CSRO are present on the local scale, Cr, Fe, Co, and Ni radii would be instead r_{Cr} = 1.264(6) Å, r_{Fe} = 1.257(5) Å, r_{Co} = 1.251(5) Å, r_{Ni} = 1.257 (5) Å, where the differences between calculated and tabulated values are relevant only for Cr and Ni.

As this assumption does not include possible changes in the alloy's effective metallic radius, EXAFS results must be discussed together with MC/MD simulation results (Table 4). In Fig. 8, MC/MD simulation results are averaged to be comparable with bond lengths experimentally determined through EXAFS. A fully disordered model (labelled noSRO in the following) is assumed when averaging the Absorber - Grey metal distances from MC/MD simulations. In the case of Cr, d(Cr-M_{noSRO}) = 2.524(11) Å. The Cr-Cr pairs have the largest interatomic distance, d(Cr-Cr) = 2.55 Å (cf. Table 4), and neglecting these bonds decreases the average bond length around Cr, resulting in d(Cr-M_{noCr}) = 2.516(5) Å. This is where the effective bond distance is expected to lie. In other words, SRO acts to decrease the Cr-*M* bond length distances, similarly to Fe-*M* distances when neglecting Fe-Fe pairs as d(Fe-M_{noSRO}) = 2.523(11) Å while d(Fe-M_{noFe}) = 2.517(4) Å.

On the other hand, Co and Ni show more homogeneous distance distributions than Cr and Fe, for which chemical short-range order will not induce appreciable variation in bond lengths. Still, Ni is the only element in the alloy which, upon alloying, changes its effective atomic radius (d(Ni-Ni) = 2.513(7) Å, r_{Ni} = 1.256(3) Å), which in turn enlarges the average Ni-*M* bond lengths compared to those expected from tabulated metallic radii estimations. Note that r_{Ni} estimated by MC/MD distances fits well with the result obtained by hard-sphere models using EXAFS and XRD data (Fig. 8).

Similarly, as reported by Zhang *et al.* [12] for the CoCrNi MEA, trials have been attempted using EXAFS data to discriminate Cr in the CoCrFeNi alloy. However, the fits are inconclusive: the nearest neighbor number of Ni atoms around Cr (and vice versa) was Cr-Ni's first nearest neighbor number (FNN) = Ni-Cr FNN = 3(2) compatibles with either a complete disorder or CSRO on both directions. As the fitting model is very likely beyond the limit of EXAFS, CSRO can only be inferred indirectly from bond distances and only from the Cr side (Cr tends to bond with smaller atoms such as Ni and Co), electronegativity, and electronic structure assumptions, as reported or calculated elsewhere [10,41,53–55] and supported by MC/MD simulations (Table 4). Neither the Debye-Waller factor of Cr, Fe, Co, and Ni at the first shell nor the Debye Temperatures (*i.e.*, a measure of thermal and static disorder extended to the fourth shell) show appreciable differences, contrary to that reported by Zhang *et al.* [12]. Another indirect evidence of the peculiar surroundings of Cr and Ni and a correlation with CSRO comes from the NEXAFS analysis performed at the L-edges and XPS analysis of the Valence Band (Fig. 9).

A NEXAFS L-edge (the 2*p* to 3*d* electron transition) spectrum of a transition metal provides information on a 3*d* band empty electron states distribution around the absorbing element above the Fermi energy [56]. Besides, according to the optical sum rules [56], the integrated normalized intensity of the L-edge resonance features is proportional to the number of electron holes at the 3*d* band, and hence, electron occupancy of the 3d band. In contrast to NEXAFS, an XPS spectrum of a transition metal (TM) VB primarily represents an energy distribution of

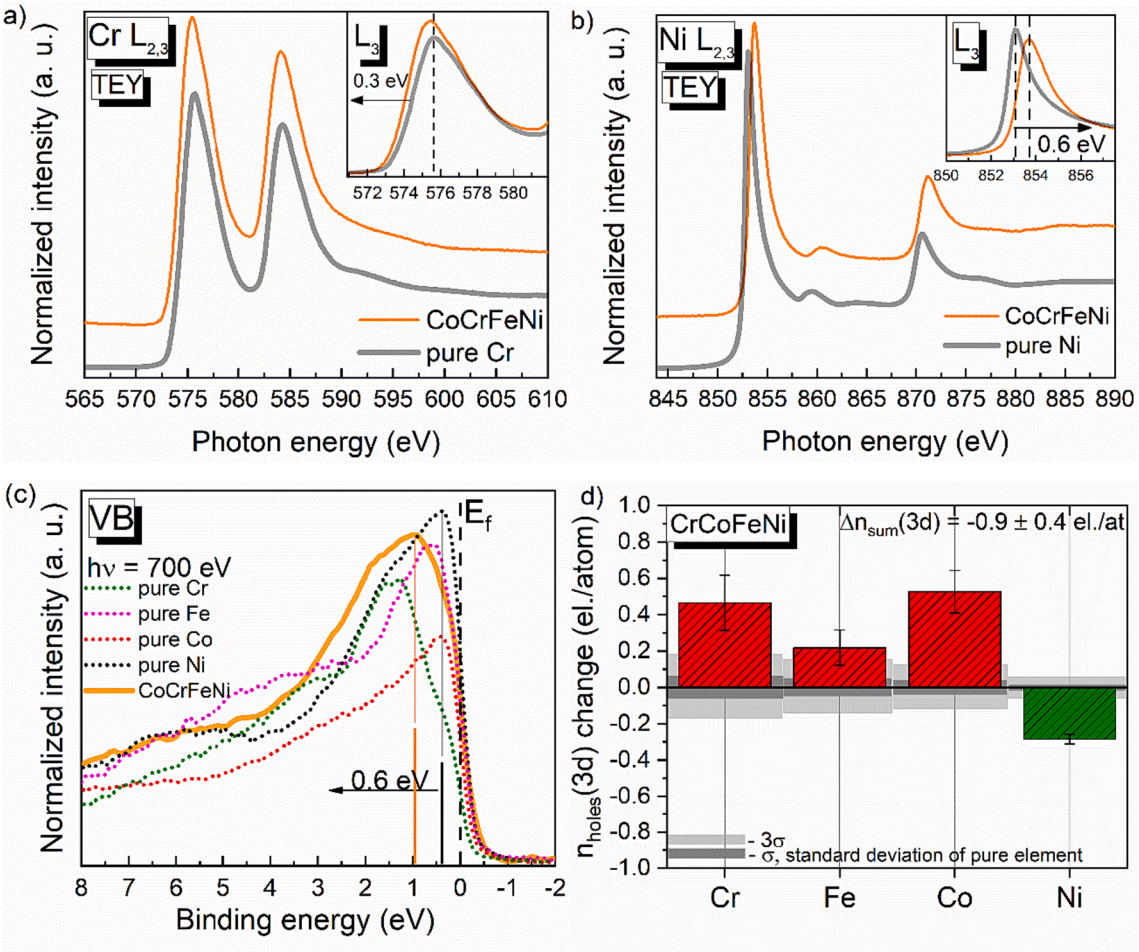

Fig. 9. NEXAFS Cr and Ni L-edges spectra recorded in TEY (a and b), XPS Valence Band spectra (c) recorded at an incident photon energy of 700 eV, and the result of the NEXAFS spectra integral intensity analysis of 3*d* electron holes number change – Δn_h(3*d*) h./atom – in CoCrFeNi (d), compared with pure elements.

occupied electron 3*d* states of the TM lying below the Fermi energy [57]. Therefore, the combination of the NEXAFS and XPS techniques allows the investigation of a TM alloy 3*d* DOS structure, which, in turn, is tightly related to the chemical interaction between constituting elements.

The Fe and Co L-edges have no energy position change relative to the spectra of the corresponding pure elements (see Fig. S4, S.M.). Furthermore, there are no differences in the $L_{2,3}$-edge energy positions between the homogenized and annealed conditions (Fig. S5, S.M.). The Ni and Cr L-edges of CoCrFeNi are shifted compared to the pure elements: Ni +0.6 eV and Cr −0.3 eV (Fig. 9a and 9b). The L-edge shifts correspond to either the energy distribution change of the empty 3*d* states (the final state of the 2*p* – 3*d* electron transition) or the core 2*p* electron levels shift (the initial state). Additional measurements of 2*p* XPS spectra revealed no significant shifts of the TMs 2*p* levels compared to the pure metals (see Fig. S6, S.M.). Hence, the observed L-edge shifts are mainly ascribed to the empty 3*d* states' energy redistribution. Given that an XPS core-line spectrum energy position is sensitive to changes in the total atomic charge of a corresponding element, one can conclude the atomic electroneutrality of the TM elements in the alloy.

The XPS VB spectrum of CoCrFeNi (Fig. 9c) reflects the total DOS distribution below E_F. However, in the studied CoCrFeNi alloy, the VB signal is dominated by the Ni and Co 3*d* photoelectrons signal due to the large photoionization cross-section of Ni and Co 3*d* states relative to other elements in the alloy [58]. Based on the cross-section values, the lowest contribution should be expected from Cr. More specifically, from theory, Co and Ni account for 72 % of the signal, followed by Fe, 20 %, and finally, Cr, 8 %. The intensity maximum of the CoCrFeNi VB spectrum appears to be shifted away from E_F by +0.6 eV compared to the VB spectra of pure Ni and Co. Previously established unchanged energy position of the empty Fe and Co 3*d* DOS maximum upon alloying allows assuming Ni as an element undergoing the occupied 3*d* DOS shift, resulting in the VB intensity maximum shift.

The observed shifts of the occupied (the VB maximum shift) and the empty (the Ni L-edge shift) 3*d* DOS maxima away from E_F imply the formation of a pseudo-gap valley in the Ni 3*d* DOS and, hence, a total DOS decrease at E_F. A Cr-Ni bonding formation can rationalize the nature of the opposite direction shifts of the Cr and Ni empty 3*d* DOS maxima, which was established from the corresponding L-edge shifts. Such energy redistribution of the 3*d* bands facilitates maximizing energy overlapping of Cr and Ni 3*d* DOS and decreases the overall bond energy. In pure Cr, both occupied and unoccupied Cr 3*d* DOS maxima are somewhat distant from E_F compared to the pure Ni 3*d* DOS, where the maxima are located almost at E_F [59].

Integral intensity analysis of the L-edge spectra thoroughly described elsewhere [53,60] has been performed to assess 3*d* band occupancy change for each element upon the CoCrFeNi alloy formation. Fig. 9d presents the change in electron holes of each TMs' 3*d* band upon alloying: $\Delta n_h(3d)$ is inversely proportional to the electrons number change $\Delta n_e(3d)$: $n_e(3d) = 10 - n_h(3d)$. Cr, Fe, and Co atoms appear to lose 3*d* electrons, while Ni atoms gain 3*d* electrons. Assuming preservation of atomic electroneutrality in the alloy – confirmed by the XPS 2*p* core-line analysis – a negative value of a total weighted average 3*d* electron number change $\Delta n_{el.sum}(3d)$ implies a total average transfer of electrons, mainly by intra-atomic transfer, from localized 3*d* states to delocalized 4*s* and 4*p* states. It is estimated that the total increase in delocalized 4*s* and 4*p* electrons upon alloy formation is 0.9(4) el./atom.

4. Discussion

4.1. Ruling out other possible sources for the anomalies

The observed anomalies on the thermophysical properties (Figs. 1 and 3) are the same as those observed for binary [5] and ternary alloys [61], which concluded the K-state transition. As mentioned in the Introduction (section 1), despite that there is no universal agreement for the occurrence of the K-state effect, proposed reasons for its appearance are the following: (*I*) atomic long-range order (LRO) [5]; (*II*) formation of Guinier-Preston zones [7]; (*III*) chemical short-range order (CSRO) [8,62]; and (*IV*) changes in electronic configuration due to local lattice distortions [9], the two last possibilities are related since CSRO may also lead to the latter. As discussed in this section, the synchrotron measurements and TEM analysis ruled out any possibility of LRO formation. The formation of GP zones is also improbable, given the results presented in the previous section that the alloy elements do not tend to bond with similar atoms. This leaves CSRO as the main possible explanation.

It should be noted that besides the K-state described above, other possible reasons for observing discontinuities in thermophysical properties are magnetic transition, recrystallization, and preferential crystallographic texture. Thus, as discussed next, the structural and microstructural characterization ruled out these possibilities by comparing as-cast and heat-treated conditions.

From Fig. 2, it is clear that a transition from a paramagnetic to a ferromagnetic state is not the reason for the observed anomalies. The Curie temperature of CrFeNi and CoCrNi MEAs and the CoCrFeNi HEA are below 110 K, far below the temperature where the discontinuities are observed. Thus, a thermal expansion anomaly that occurs at the Curie temperature, such as that observed for Invar alloys, is discarded as a probable cause.

Recrystallization has been reported to cause a similar anomaly in the CTE(T) of low-carbon steels [63] at the same temperature range observed in Fig. 1. However, the samples were as-cast in the present study, with no driving force for recrystallization. The only effect expected upon heating is grain growth, as revealed in Fig. 6. Grain growth does not necessarily cause CTE(T) discontinuities since it would generally be observed for other alloys. From the IPFs shown in Fig. 6, it is concluded that texture does not relate to the observed discontinuities.

Lattice parameter contractions of ~0.05 % were reported for $Ni_{75}Cr_{25}$ (wt. %) alloy upon aging at and below 823 K for 24 h [5]. The lattice parameter contraction occurs because of the formation of CSRO in $Ni_{75}Cr_{25}$ alloy, ascertained based on TEM results and increased electrical resistivity (0.4 %) upon annealing. The maximum lattice parameter difference in the CoCrFeNi alloy, measured by XRD (Table 3) for the as-cast and heat-treated samples, is ~0.08 %. Contrary to what is reported in Ref. [5], a lattice parameter expansion upon aging and annealing is observed. However, the observed changes are less than the measurement error. It is also corroborated by the interatomic distances of each element of the CoCrFeNi HEA for the three differently heat-treated specimens using a binary model Absorber - Grey Metal, shown in Fig. S7 in the S.M. However, considering the calculated margin of error, the lattice parameters derived from the synchrotron XRD data are equal and do not allow further interpretation.

Synchrotron XRD (Fig. 5) and TEM results (Fig. 7) confirm that a second phase precipitation does not occur in the CoCrFeNi alloy during the heat treatments, which was much longer than the time of the thermophysical measurements. Hence, magnetic transitions, phase precipitation, texture, and recrystallization are eliminated as probable causes for the anomalies observed on the temperature-dependent physical properties of the CoCrFeNi alloy (Figs. 1 and 3).

The weak diffuse intensities from the TEM images (Fig. 7g to 7j) at the $^1/_3\{422\}$ and $½\{311\}$ directions under the [111] and [112] zone axes were observed for both homogenized and aged conditions. Although these extra intensities have been consistently linked to CSRO in the literature [13,27,64–66], the origin of these reflections is still controversial [67], as they are also present in other materials such as in pure Cu [14], we do not assume that the extra reflections to be a direct observation of CSRO [68].

Finally, a minimum observed in the first heating cycles in both CTE (Fig. 1) and $c_p(T)$ (Fig. 3) for as-cast samples, and again visible in the DSC curve of the homogenized CoCrFeNi alloy (~740 K, Fig. 10a and 10b) and the $c_p(T)$ (Fig. 10c), cannot be due to the annihilation of

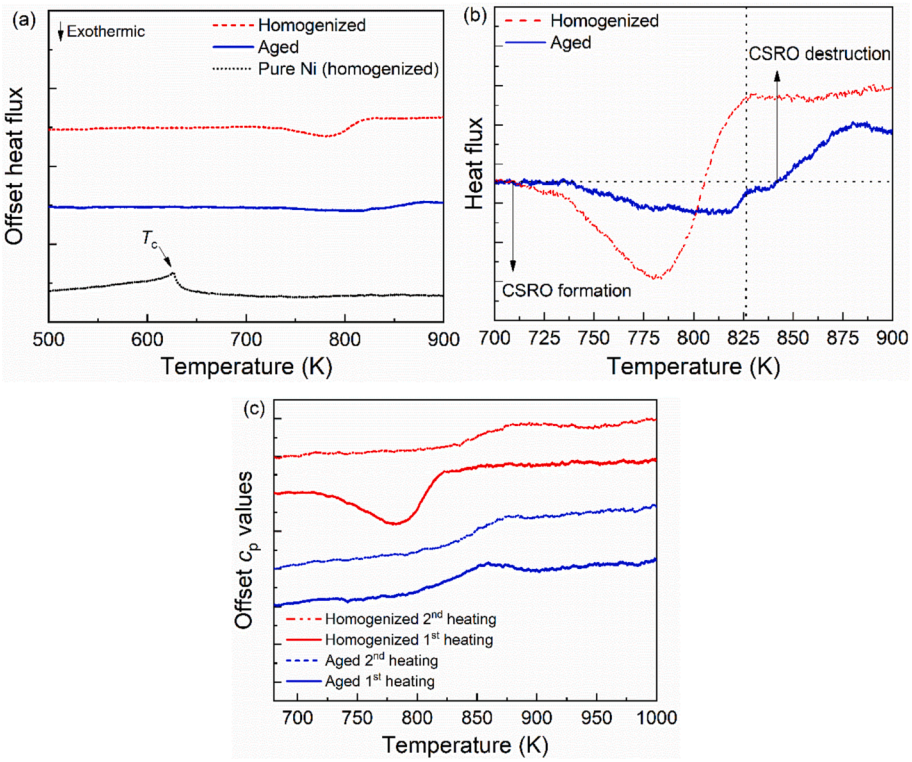

Fig. 10. (a) The DSC curves of CoCrFeNi in homogenized and aged conditions. Homogenized pure Ni is added for comparison; (b) inset of (a) evidencing the formation and destruction of chemical short-range order upon heating; (c) the $c_p(T)$ of homogenized and aged samples of CoCrFeNi HEA in the first and second heating cycles.

vacancies and defects from non-equilibrium solidification. To rule out this possibility, a homogenized pure Ni sample DSC curve was also measured and is presented in Fig. 10a. As shown, no transition is observed in pure Ni (homogenized) in the 700–900 K temperature range, even though the sample preparation method was rigorously the same as that of the CoCrFeNi HEA. Thus, by ruling out all other possibilities, we can attribute the anomalies from 700 to 900 K to the formation and/or destruction of CSRO, as will be discussed next.

4.2. CSRO formation on CoCrFeNi

First, it should be noted that the temperatures for the anomalies observed described here match computational simulations reported in the literature. The peak maximum in the $c_p(T)$ of the CoCrNi alloy (Fig. 3), determined experimentally in this study, is 910 K on the first heating and 920 K on the second heating cycle. These experimental results agree with the predicted value (975 K), employing *ab initio* calculations and on-lattice machine learning interatomic potentials in Ref. [24]. In the dilatometry measurement (CoCrNi – Fig. 1a), the inset is 800 K, and the end temperature is 935 K on the first heating. For CrFeNi and CoCrFeNi alloys, the start and end temperatures are slightly lower than CoCrNi (Fig. 1a).

On the DSC curves (Fig. 10b), the anomaly can be described as a decrease in the heat flux (indicating an exothermic reaction) with an onset at around 700 K followed by a sharp increase at around 825 K. It should be noted that this thermal event is much less intense on the second heating of as-cast samples (Figs. 1 and 3) and on the aged sample shown in Fig. 10a, which besides the 10 h aging at 773 K, experienced a slow cooling on the furnace. The temperature profile of the 773 K aging heat treatment is shown in Fig. S8 in the S.M.

Based on the theoretical times for CSRO development [17], the homogenized and cast condition should develop far less CSRO than the aged sample. This is because the former experiences a high cooling rate from a high temperature, which hinders the CSRO formation. It occurs because the ordered state has a more negative enthalpy and less entropy, so it is favored at lower temperatures and occurs after an exothermic event. Its destruction should, therefore, be endothermic. In agreement with this explanation, when the homogenized sample is slowly heated (10 K • min^{-1}), reaching the 750–825 K temperature range, CSRO starts to develop, leading to an exothermic event on the DSC curves (Figs. 1, 3, and 10). In this temperature range, the CSRO should develop within minutes [17]. As temperature increases, we eventually reach a temperature at which CSRO should start being destroyed. Based on the DSC curves (Fig. 10a and 10b), we expect that the temperature is strictly at around 825 K for this heating rate. At this temperature, CSRO stops forming and should also start being destroyed, which leads to a sharp increase in the heat flux since the overall reaction is endothermic.

On the other hand, aging for 10 h at 773 K, followed by slow cooling, should significantly increase the amount of CSRO. Again, in agreement with this, as shown in Fig. 10a and 10b, the exothermic event is much subtler as the samples are saturated. Nonetheless, the increase predicted to be the start of the decrease of CSRO can be observed.

The fact that the exothermic event is also subtle on the 2nd heating in the $c_p(T)$ curves, as shown in Fig. 10c, suggests that the cooling performed on the DSC (10 K • min^{-1}) is sufficiently low to induce a higher amount of CSRO than the rapidly cooled sample. It means that if the explanation proposed here is correct, upon cooling on the DSC, a decrease in the heat flux should start to occur at the same temperature range (750–800 K). Indeed, when the cooling curve reaches this temperature, the baseline line of the curves is shifted downwards, indicating the beginning of an exothermic reaction as shown in Fig. 11b. The similar DSC heating–cooling curves for the aged condition are shown in Fig. S9 in the S.M. This combination of results proves that the observed phenomenon is reversible and agrees with what would be expected for a CSRO reaction.

A schematic time–temperature-transformation dependence of CSRO

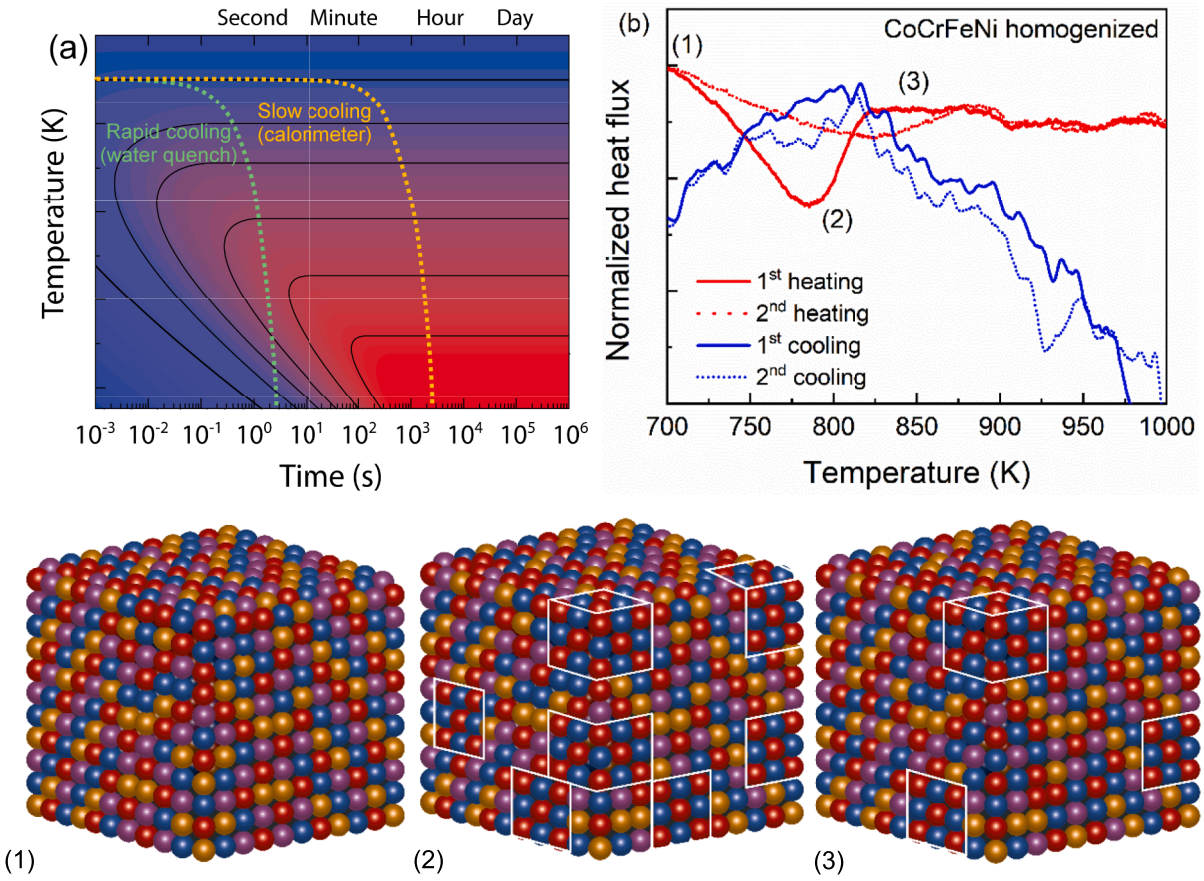

Fig. 11. (a) Schematic temperature-dependence of chemical short-range transition in CoCrFeNi; (b) the normalized DSC signals of the homogenized condition. The heating and cooling rates were 10 K • min^{-1}; (1), (2), and (3) are schematic representations of the temperature-dependent atomic configurations of the CoCrFeNi HEA marked in (b).

is shown in Fig. 11a based on the theoretical calculations done by Du *et al.* [17]. The blue–red color code represents the degree of order, red is a higher degree, and the lines represent the cooling rates in the DSC (Figs. 10 and 11b) and water-quenched samples. The atom boxes represent the three different temperature-dependent states in Fig. 11b; (1) more random solid solution (or with minimal CSRO); (2) increased amount of CSRO; and (3) destruction of some of the CSRO from the previous state.

It should be noted that these results do not imply that the rapidly cooled samples, or when at temperatures higher than 900 K, the alloys do not display any degree of CSRO. It only means slow cooling and/or aging at low temperatures intensifies it. On the other hand, the observed CSRO does not develop into LRO for any of the conditions studied in this study (Figs. 5 and 7). For comparison, in multiple Ni-based superalloys, LRO occurs even on rapid cooling, forming a nanometric $L1_2$ phase [69].

The reported annealing temperatures for the CoCrNi MEA vary between 673 K [14] and 1273 K [13]. However, as a diffusion-dependent transformation, the order–disorder transition should depend on both time and temperature and the equilibrium vacancy concentration, as demonstrated by computational means in Refs. [17,27]. Recently, Li *et al.* [14] studied the evolution of CSRO in the CoCrNi alloy by monitoring the electrical resistivity variance for different annealing temperatures and times. Higher temperatures (973 K) required less time to reach the electrical resistivity saturation, whereas lower temperatures (773 K) had a higher saturation value. Annealing at 673 K revealed that a saturation value was not reached even after 500 h. Similar behavior is reported for Cr-Ni alloys [61], where a first-order phase transformation, governed by nucleation and growth of ordered clusters in the matrix, results in CSRO. The nucleation rate increases with decreasing temperature, while the growth rate decreases with increasing temperature because it depends on atomic diffusion.

Cr and Ni elements have peculiar characteristics in most of the 3*d*-based alloys investigated, and in CoCrFeNi, they have the lowest and highest Z correlated with most different electronegativity (Cr 1.66, Ni 1.91 Pauling scale), lowest Miedema mixing enthalpy (ΔH_{mix} Cr-Ni = -7 kJ mol^{-1}). It is not new that they tend to have bonding preferences in *fcc* structures [12,41,53,70], from which we expect that in the CoCrFeNi alloy, some degree of CSRO is present and it is confirmed by MC/MD simulations. By combining EXAFS and MC/MD, CSRO explains also the shorter Cr-*M* distances shown in Fig. 8, as the Cr-Cr bond, having the largest bond distance, is disfavored.

The Cr-Cr pair correlation functions as per the distance *r* (Å) show a two-peak structure, as presented in Fig. S10 (inset, S. M.). The double peak is likely a direct consequence of the orientations of magnetic moments. Every Co, Fe, and Ni atom favors moments aligned with its neighbors, while Cr favors anti-alignment. When Cr atoms are nearest neighbors, they are frustrated because they both prefer to orient opposite to the surrounding Co, Fe, and Ni, but this forces them to align with each other. This creates a strong energy preference for not sitting within its first nearest neighbor shell [71]. An effect in magnetism known as the Bethe-Slater curve shows that antiferromagnetism is favored at short interatomic spacings, while ferromagnetism is favored at large spacings. Consequently, frustrated Cr can relieve frustration by moving to larger spacings, as depicted in Fig. S11 in the S.M. The overall effect is that CSRO is largest around Cr atoms: on top of unfavored Cr-Cr bonds, those existing have a wide bond length distribution, visible as the most significant standard deviation for any atomic pairs in Table 4 (±0.03 Å). Overall, Cr-*M* distances are reduced by magnetic frustration and

subsequent chemical short-range order, while Ni-*M* distances are mainly increased by changes in the effective Ni metallic radius upon alloying. Finally, from pair correlation data, Cr tends to avoid Cr and bond to ferromagnetic and smaller Co and Ni, and Fe tends to avoid Fe and bond to smaller Co and Ni. Reversely, Co and Ni tend to bond to larger Cr and Fe. Ghosh *et al.* [24], using canonical MC simulations, concluded that the ordering of Cr atoms is mostly responsible for the high-temperature phase transition that is represented by a peak in the specific heat curve at 975 K.

Another peculiar behavior around Cr and Ni elements arises from XAS and XPS (Figs. 8 and 9) by observing the NEXAFS Ni and Cr L-edge spectra (unoccupied 3*d* DOS) and the XPS valence band spectrum (occupied 3*d* DOS). Based on the spectra analysis, a peculiar redistribution of Cr and Ni 3d DOS upon alloying was established, suggesting chemical interaction of Cr and Ni resulting in splitting of the Ni 3d band at E_F and, hence, overall pseudo-gap formation in the total DOS of the alloys. The findings are in line with the prediction of CSRO by Tamm *et al.* [10] that inferred 3*d* DOS close to E_F shows the formation of a pseudo-gap valley upon alloying, which is observed experimentally, to our knowledge, for the first time for the CoCrFeNi alloy in the present study.

It is essential to note that, although the findings by Tamm *et al.* [10] showed a clear correlation between CSRO and pseudo-gap formation, the DOS calculations were performed there at 500 K, which suggests a highly ordered state of the alloy. In the current work, the electronic structure of the alloy was analyzed at 773 K and 1473 K. As discussed previously, as we can assume less ordering with temperature increase, the alloy state simulated by Tamm *et al.* and those studied in the current work formally cannot be considered identical to each other. Therefore, the assumption of the correlation between the pseudo-gap and short-range order presence being valid for the alloy at a state of higher temperature is an extrapolation.

This study points in the direction of the formation of CSRO upon heating–cooling cycles during the thermophysical measurements of the CoCrNi and CoCrFeNi alloys. All other possibilities (magnetic transition, second-phase precipitation, texture, recrystallization, and LLD) have been considered, investigated, and disregarded. Furthermore, EXAFS, NEXAFS, and XPS corroborate the conclusion with evidence of CSRO, detailed previously, while direct evidence comes from MC/MD simulations on the homogenized CoCrFeNi (see Table 4), which reveal the formation of CSRO on MEA and HEAs. Even though synchrotron XRD [72] and TEM [67] have spatial resolution limitations that do not allow a conclusion about the formation of CSRO in the CoCrFeNi HEA, MC/MD, XAS, and XPS give more confident results about CSRO in the CoCrFeNi HEA. The conclusion is further supported by indirect evidence of anomalies in the thermophysical properties (Figs. 1, 3, 10, and 11).

The results indicate that physical measurements are invaluable tools for identifying and characterizing CSRO in HEAs. These materials exhibit similar behaviors to conventional, more dilute alloys. From a future perspective, the authors suggest *in situ* heating–cooling cycles during synchrotron XRD or neutron diffraction, monitoring lattice parameter variations (excluding thermal effects) in the temperature of interest (indirect evidence of CSRO).

5. Conclusion

In this study, measurements of the coefficient of thermal expansion and specific heat capacity of high-entropy (CoCrFeNi) and medium-entropy (CoCrNi and CrFeNi) alloys have revealed reversible anomalies in the 600–950 K temperature range. The first heating cycle of as-cast and homogenized samples shows a steep valley followed by a sudden increase in both CTE and c_p, whereas the second heating cycle and for aged samples only showed an increase in CTE and c_p is observed in the same temperature range. Magnetic measurements indicate that the phenomenon cannot be attributed to magnetic transitions, and microstructural analysis eliminates second-phase precipitation and recrystallization as possible causes.

The combination of results from TEM, synchrotron XRD and XAS finally indicates that the anomalies are attributed to a diffusional local chemical ordering process during heating and cooling cycles. X-ray absorption and photoelectron spectroscopies provided local structural evidence, *e.g.*, a pseudo-gap valley in the Density of States and differences between calculated and tabulated atomic radii for Cr and Ni, indicating a higher affinity of Ni and Cr, more direct evidence of CSRO. The results are nicely corroborated by MC/MD simulations.

By comparing slowly cooled to quenched specimens, one creates different degrees of CSRO, which are finally resolved above the K-state temperature region, between 700 and 900 K. Even though these subtle differences are invisible experimentally using techniques such as synchrotron XRD, TEM, and EXAFS, differential scanning calorimetry can grasp two temperature regions, one (*ca.* 700–800 K) associated with CSRO development and another (*ca.* 800–900 K) associated with CSRO destruction, corroborating simulation-based results reported in the literature at different temperatures.

Notably, the study suggests that more straightforward and cost-effective indirect methods, such as differential scanning calorimetry (DSC) and dilatometry, can be more practical and effective than the more complex techniques, such as synchrotron X-ray diffraction, scanning, and transmission electron microscopy for determining CSRO in these alloys.

CRediT authorship contribution statement

Angelo F. Andreoli: Writing – review & editing, Writing – original draft, Visualization, Validation, Project administration, Methodology, Investigation, Funding acquisition, Formal analysis, Data curation, Conceptualization. **Andrea Fantin:** Writing – review & editing, Writing – original draft, Visualization, Validation, Methodology, Investigation, Funding acquisition, Formal analysis, Data curation, Conceptualization. **Sergey Kasatikov:** Writing – review & editing, Writing – original draft, Visualization, Validation, Methodology, Investigation, Funding acquisition, Formal analysis, Data curation, Conceptualization. **Vinícius P. Bacurau:** Writing – original draft, Methodology, Investigation, Formal analysis, Conceptualization. **Michael Widom:** Writing – review & editing, Software, Resources, Methodology, Investigation, Formal analysis. **Piter Gargarella:** Writing – review & editing, Supervision, Resources. **Eric M. Mazzer:** Writing – review & editing, Validation. **Thomas G. Woodcock:** Resources, Formal analysis. **Kornelius Nielsch:** Writing – review & editing, Supervision, Funding acquisition. **Francisco G. Coury:** Writing – review & editing, Visualization, Validation, Supervision, Resources, Project administration, Methodology, Investigation, Funding acquisition, Formal analysis.

Declaration of competing interest

The authors declare that they have no known competing financial interests or personal relationships that could have appeared to influence the work reported in this paper.

Data availability

Data will be made available on request.

Acknowledgments

A.F.A. acknowledges the financial support as a Postdoctoral fellow, grant 2021/12056-7, São Paulo Research Foundation (FAPESP). A.F. acknowledges the financial support by the Deutsche Forschungsgemeinschaft project FA1817/1-2. S.K. acknowledges the financial support by the Deutsche Forschungsgemeinschaft (project GL181/57-2, FA1817/1-2) and Helmholtz Initiative for Refugees, funded by the Initiative and Networking Fund of the President of the

Helmholtz Association. V.P.B. acknowledges the financial support as a Master's degree scholarship, grant 2022/12641-0, FAPESP. M.W. was supported by the Department of Energy under Grant No. DE-SC0014506. This research also used the resources of the National Energy Research Scientific Computing Center (NERSC), a US Department of Energy Office of Science User Facility operated under contract number DE-AC02-05CH11231 using NERSC award BES-ERCAP24744. F.G.C. acknowledges the financial support from FAPESP, grant 2022/02770-7. The research was sponsored by the Army Research Office and was accomplished under Grant Number W911NF-23-1-0310. The views and conclusions contained in this document are those of the authors and should not be interpreted as representing the official policies, either expressed or implied, of the Army Research Office or the U.S. Government. The U. S. Government is authorized to reproduce and distribute reprints for Government purposes notwithstanding any copyright notation herein. The authors thank Dr. Ivan Kaban (IFW-Dresden) for the discussions. We thank Mrs. Birgit Bartusch (IFW-Dresden) for part of the DSC measurements and Dr. Torsten Mix for the magnetic moment measurements. We acknowledge DESY (Hamburg, Germany), a member of the Helmholtz Association HGF, for providing experimental facilities. Parts of this research were carried out at PETRA III, beamline P02.1, at DESY. The authors thank Helmholtz-Zentrum Berlin for providing beamtime at BESSYII and Dmitry Smirnov for the experiment support at the RGBL station.

Appendix A. Supplementary data

Supplementary data to this article can be found online at https://doi.org/10.1016/j.matdes.2024.112724.

References

[1] H. Thomas, Über Widerstandslegierungen, Z. Phys. 129 (1951) 219–232, https://doi.org/10.1007/BF01333398.
[2] R.G. Davies, An X-ray and dilatometric study of order and the "K-state" in iron-aluminum alloys, J. Phys. Chem. Solid 24 (1963) 985–992, https://doi.org/10.1016/0022-3697(63)90002-7.
[3] W. Bendick, H.H. Ettwig, W. Pepperhoff, Anomalies in specific heat and thermal expansion of FCC iron alloys, J. Phys. F: Metal Phys. 8 (1978) 2525–2534, https://doi.org/10.1088/0305-4608/8/12/012.
[4] B.H. Rabin, W.D. Swank, R.N. Wright, Thermophysical properties of Alloy 617 from 25°C to 1000°C, Nucl. Eng. Des. 262 (2013) 72–80, https://doi.org/10.1016/j.nucengdes.2013.03.048.
[5] A. Marucco, B. Nath, Effects of ordering on the properties of Ni-Cr alloys, J. Mater. Sci. 23 (1988) 2107–2114, https://doi.org/10.1007/BF01115776.
[6] E. Lang, V. Lupinc, A. Marucco, Effect of thermomechanical treatments on short-range ordering and secondary-phase precipitation in Ni-Cr-based alloys, Mater. Sci. Eng. A 114 (1989) 147–157, https://doi.org/10.1016/0921-5093(89)90853-8.
[7] E.A. Starke, V. Gerold, A.G. Guy, An investigation of the k-effect in Nickel-Aluminum alloys, Acta Metall. 13 (1965) 957–964, https://doi.org/10.1016/0001-6160(65)90003-9.
[8] E.E. Stansbury, C.R. Brooks, T.L. Arledge, Specific-heat anomalies in solid solutions of chromium and molybdenum in nickel: evidence for short-range order, J. Inst. Met. 94 (1966) 136.
[9] H.J. Logie, J. Jackson, J.C. Anderson, F.R.N. Nabarro, Effect of plastic deformation on resistivity of gold-palladium alloys, Acta Metall. 9 (1961) 707–713, https://doi.org/10.1016/0001-6160(61)90100-6.
[10] A. Tamm, A. Aabloo, M. Klintenberg, M. Stocks, A. Caro, Atomic-scale properties of Ni-based FCC ternary, and quaternary alloys, Acta Mater. 99 (2015) 307–312, https://doi.org/10.1016/j.actamat.2015.08.015.
[11] Z. Pei, R. Li, M.C. Gao, G.M. Stocks, Statistics of the NiCoCr medium-entropy alloy: Novel aspects of an old puzzle, npj Comput. Mater. 6 (2020) 122, https://doi.org/10.1038/s41524-020-00389-1.
[12] F.X. Zhang, S. Zhao, K. Jin, H. Xue, G. Velisa, H. Bei, R. Huang, J.Y.P.P. Ko, D. C. Pagan, J.C. Neuefeind, W.J. Weber, Y. Zhang, Local structure and short-range order in a NiCoCr solid solution alloy, Phys. Rev. Lett. 118 (2017) 1–6, https://doi.org/10.1103/PhysRevLett.118.205501.
[13] R. Zhang, S. Zhao, J. Ding, Y. Chong, T. Jia, C. Ophus, M. Asta, R.O. Ritchie, A. M. Minor, Short-range order and its impact on the CrCoNi medium-entropy alloy, Nature 581 (2020) 283–287, https://doi.org/10.1038/s41586-020-2275-z.
[14] L. Li, Z. Chen, S. Kuroiwa, M. Ito, K. Yuge, K. Kishida, H. Tanimoto, Y. Yu, H. Inui, E.P. George, Evolution of short-range order and its effects on the plastic deformation behavior of single crystals of the equiatomic Cr-Co-Ni medium-entropy alloy, Acta Mater. 243 (2023) 118537, https://doi.org/10.1016/j.actamat.2022.118537.
[15] F.G. Coury, C. Miller, R. Field, M. Kaufman, On the origin of diffuse intensities in fcc electron diffraction patterns, Nature 622 (2023) 742–747, https://doi.org/10.1038/s41586-023-06530-6.
[16] K. Inoue, S. Yoshida, N. Tsuji, Direct observation of local chemical ordering in a few nanometer range in CoCrNi medium-entropy alloy by atom probe tomography and its impact on mechanical properties, Phys Rev Mater 5 (2021) 085007, https://doi.org/10.1103/PhysRevMaterials.5.085007.
[17] J.-P. Du, P. Yu, S. Shinzato, F.-S. Meng, Y. Sato, Y. Li, Y. Fan, S. Ogata, Chemical domain structure and its formation kinetics in CrCoNi medium-entropy alloy, Acta Mater. 240 (2022) 118314, https://doi.org/10.1016/j.actamat.2022.118314.
[18] B. Yin, S. Yoshida, N. Tsuji, W.A. Curtin, Yield strength and misfit volumes of NiCoCr and implications for short-range-order, Nat. Commun. 11 (2020) 2507, https://doi.org/10.1038/s41467-020-16083-1.
[19] Q.-J. Li, H. Sheng, E. Ma, Strengthening in multi-principal element alloys with local-chemical-order roughened dislocation pathways, Nat. Commun. 10 (2019) 3563, https://doi.org/10.1038/s41467-019-11464-7.
[20] J. Ding, Q. Yu, M. Asta, R.O. Ritchie, Tunable stacking fault energies by tailoring local chemical order in CrCoNi medium-entropy alloys, Proc. Natl. Acad. Sci. USA 115 (2018) 8919–8924. doi: 10.1073/pnas.1808660115.
[21] K. Jin, B.C. Sales, G.M. Stocks, G.D. Samolyuk, M. Daene, W.J. Weber, Y. Zhang, H. Bei, Tailoring the physical properties of Ni-based single-phase equiatomic alloys by modifying the chemical complexity, Sci. Rep. 6 (2016) 20159, https://doi.org/10.1038/srep20159.
[22] K. Jin, S. Mu, K. An, W.D. Porter, G.D. Samolyuk, G.M. Stocks, H. Bei, Thermophysical properties of Ni-containing single-phase concentrated solid solution alloys, Mater. Des. 117 (2017) 185–192, https://doi.org/10.1016/j.matdes.2016.12.079.
[23] T. Teramoto, K. Kitasumi, R. Shimohara, Y. Ito, R. Shimizu, K. Tanaka, R. Ueji, Formation condition and effect on the early stages of plastic deformation of chemical short-range order in Cr-Co-Ni medium-entropy alloy, J. Alloy. Compd. 941 (2023) 169016, https://doi.org/10.1016/j.jallcom.2023.169016.
[24] S. Ghosh, V. Sotskov, A.V. Shapeev, J. Neugebauer, F. Körmann, Short-range order and phase stability of CrCoNi explored with machine learning potentials, Phys Rev Mater 6 (2022) 113804, https://doi.org/10.1103/PhysRevMaterials.6.113804.
[25] E. Antillon, C. Woodward, S.I. Rao, B. Akdim, T.A. Parthasarathy, Chemical short range order strengthening in a model FCC high entropy alloy, Acta Mater. 190 (2020) 29–42, https://doi.org/10.1016/j.actamat.2020.02.041.
[26] C.G. Schön, On short-range order strengthening and its role in high-entropy alloys, Scr. Mater. 196 (2021) 113754, https://doi.org/10.1016/j.scriptamat.2021.113754.
[27] L. Zhou, Q. Wang, J. Wang, X. Chen, P. Jiang, H. Zhou, F. Yuan, X. Wu, Z. Cheng, E. Ma, Atomic-scale evidence of chemical short-range order in CrCoNi medium-entropy alloy, Acta Mater. 224 (2022) 117490, https://doi.org/10.1016/j.actamat.2021.117490.
[28] ASTM E 1269-11, Standard Test Method for Determining Specific Heat Capacity by Differential Scanning Calorimetry, American Society for Testing and Materials, 2011.
[29] T. Degen, M. Sadki, E. Bron, U. König, G. Nénert, The high score suite, Powder Diffr. (2014), https://doi.org/10.1017/S0885715614000840.
[30] I. Zizak, P. Gaal, The KMC-3 XPP beamline at BESSY II, J. Large-Scale Res. Facil. JLSRF 3 (2017) A123, https://doi.org/10.17815/jlsrf-3-112.
[31] G. Schuck, I. Zisak, CryoEXAFS: X-ray absorption spectroscopy station with cryogenic or in-beam operando electrochemistry sample conditions at BESSY II, J. Large-Scale Res. Facil. JLSRF 6 (2020) 139, https://doi.org/10.17815/jlsrf-6-176.
[32] M. Widom, W.P. Huhn, S. Maiti, W. Steurer, Hybrid Monte Carlo/molecular dynamics simulation of a refractory metal high entropy alloy, Metall. Mater. Trans. A 45 (2014) 196–200, https://doi.org/10.1007/s11661-013-2000-8.
[33] G. Kresse, J. Furthmüller, Efficient iterative schemes for ab initio total-energy calculations using a plane-wave basis set, Phys. Rev. B 54 (1996) 11169–11186, https://doi.org/10.1103/PhysRevB.54.11169.
[34] G. Kresse, D. Joubert, From ultrasoft pseudopotentials to the projector augmented-wave method, Phys. Rev. B 59 (1999) 1758–1775, https://doi.org/10.1103/PhysRevB.59.1758.
[35] J.P. Perdew, K. Burke, M. Ernzerhof, Generalized gradient approximation made simple, Phys. Rev. Lett. 77 (1996) 3865–3868, https://doi.org/10.1103/PhysRevLett.77.3865.
[36] N. Norman, B.E. Warren, X-ray measurement of short range order in Ag-Au, J. Appl. Phys. 22 (1951) 483–486, https://doi.org/10.1063/1.1699988.
[37] J.M. Cowley, Short-range order and long-range order parameters, Phys. Rev. 138 (1965) A1384–A1389, https://doi.org/10.1103/PhysRev.138.A1384.
[38] G. Laplanche, P. Gadaud, C. Bärsch, K. Demtröder, C. Reinhart, J. Schreuer, E. P. George, Elastic moduli and thermal expansion coefficients of medium-entropy subsystems of the CrMnFeCoNi high-entropy alloy, J. Alloy. Compd. 746 (2018) 244–255, https://doi.org/10.1016/j.jallcom.2018.02.251.
[39] G. Laplanche, M. Schneider, F. Scholz, J. Frenzel, G. Eggeler, J. Schreuer, Processing of a single-crystalline CrCoNi medium-entropy alloy and evolution of its thermal expansion and elastic stiffness coefficients with temperature, Scr. Mater. 177 (2020) 44–48, https://doi.org/10.1016/j.scriptamat.2019.09.020.
[40] H. Ge, H. Song, J. Shen, F. Tian, Effect of alloying on the thermal-elastic properties of 3d high-entropy alloys, Mater. Chem. Phys. 210 (2018) 320–326, https://doi.org/10.1016/j.matchemphys.2017.10.046.
[41] A. Fantin, G.O. Lepore, A.M. Manzoni, S. Kasatikov, T. Scherb, T. Huthwelker, F. D'Acapito, G. Schumacher, Short-range chemical order and local lattice distortion in a compositionally complex alloy, Acta Mater. 193 (2020) 329–337, https://doi.org/10.1016/j.actamat.2020.04.034.

[42] J.J. Rehr, R.C. Albers, Theoretical approaches to X-ray absorption fine structure, Rev. Mod. Phys. 72 (2000) 621–654, https://doi.org/10.1103/RevModPhys.72.621.
[43] F. Zhang, Y. Tong, K. Jin, H. Bei, W. Weber, Y. Zhang, Lattice distortion and phase stability of Pd-doped NiCoFeCr solid-solution alloys, Entropy 20 (2018) 900, https://doi.org/10.3390/e20120900.
[44] Y. Tong, K. Jin, H. Bei, J.Y.P. Ko, D.C. Pagan, Y. Zhang, F.X. Zhang, Local lattice distortion in NiCoCr, FeCoNiCr and FeCoNiCrMn concentrated alloys investigated by synchrotron X-ray diffraction, Mater. Des. 155 (2018) 1–7, https://doi.org/10.1016/j.matdes.2018.05.056.
[45] S. San, Y. Tong, H. Bei, B. Kombaiah, Y. Zhang, W.-Y. Ching, First-principles calculation of lattice distortions in four single phase high entropy alloys with experimental validation, Mater. Des. 209 (2021) 110071, https://doi.org/10.1016/j.matdes.2021.110071.
[46] L.R.R. Owen, E.J.J. Pickering, H.Y.Y. Playford, H.J.J. Stone, M.G.G. Tucker, N.G. G. Jones, An assessment of the lattice strain in the CrMnFeCoNi high-entropy alloy, Acta Mater. 122 (2017) 11–18, https://doi.org/10.1016/j.actamat.2016.09.032.
[47] Y.F.F. Ye, Y.H.H. Zhang, Q.F.F. He, Y. Zhuang, S. Wang, S.Q.Q. Shi, A. Hu, J. Fan, Y. Yang, Atomic-scale distorted lattice in chemically disordered equimolar complex alloys, Acta Mater. 150 (2018) 182–194, https://doi.org/10.1016/j.actamat.2018.03.008.
[48] Y. Tong, S. Zhao, H. Bei, T. Egami, Y. Zhang, F. Zhang, Severe local lattice distortion in Zr- and/or Hf-containing refractory multi-principal element alloys, Acta Mater. 183 (2020) 172–181, https://doi.org/10.1016/j.actamat.2019.11.026.
[49] G.Y. Guo, H.H. Wang, Calculated elastic constants and electronic and magnetic properties of bcc, fcc, and hcp Cr crystals and thin films, Phys. Rev. B 62 (2000) 5136–5143, https://doi.org/10.1103/PhysRevB.62.5136.
[50] Z.S.B.W. Hume-Rothery, A.L. Sutton, The lattice expansion of iron, Proc. R. Soc. Lond. A., Math. Phys. Sci. 229 (1955) 459–467.
[51] A. Taylor, R.W. Floyd, Precision measurements of lattice parameters of non-cubic crystals, Acta Crystallogr. 3 (1950) 285–289, https://doi.org/10.1107/S0365110X50000732.
[52] I.-K. Suh, H. Ohta, Y. Waseda, High-temperature thermal expansion of six metallic elements measured by dilatation method and X-ray diffraction, J. Mater. Sci. 23 (1988) 757–760, https://doi.org/10.1007/BF01174717.
[53] S. Kasatikov, A. Fantin, A.M. Manzoni, S. Sakhonenkov, A. Makarova, D. Smirnov, E.O. Filatova, G. Schumacher, Chemical interaction and electronic structure in a compositionally complex alloy: A case study by means of X-ray absorption and X-ray photoelectron spectroscopy, J. Alloy. Compd. 857 (2021) 157597, https://doi.org/10.1016/j.jallcom.2020.157597.
[54] H.S. Oh, K. Odbadrakh, Y. Ikeda, S. Mu, F. Körmann, C.-J. Sun, H.S. Ahn, K. N. Yoon, D. Ma, C.C. Tasan, T. Egami, E.S. Park, Element-resolved local lattice distortion in complex concentrated alloys: An observable signature of electronic effects, Acta Mater. 216 (2021) 117135, https://doi.org/10.1016/j.actamat.2021.117135.
[55] Y. Ikeda, B. Grabowski, F. Körmann, Ab initio phase stabilities and mechanical properties of multicomponent alloys: A comprehensive review for high entropy alloys and compositionally complex alloys, Mater Charact 147 (2019) 464–511, https://doi.org/10.1016/j.matchar.2018.06.019.
[56] J. Stöhr, NEXAFS Spectroscopy, Springer, Berlin, Heidelberg, 1992 doi: 10.1007/978-3-662-02853-7.
[57] B.V. Senkovskiy, D.Y. Usachov, A.V. Fedorov, O.Y. Vilkov, A.V. Shelyakov, V. K. Adamchuk, Electronic structure of Ti–Ni alloys: An XPS and NEXAFS study, J. Alloy. Compd. 537 (2012) 190–196, https://doi.org/10.1016/j.jallcom.2012.05.059.
[58] J.J. Yeh, I. Lindau, Atomic subshell photoionization cross sections and asymmetry parameters: 1 ⩽ Z ⩽ 103, At. Data Nucl. Data Tables 32 (1985) 1–155, https://doi.org/10.1016/0092-640X(85)90016-6.
[59] D.A. Papaconstantopoulos, Handbook of the Band Structure of Elemental Solids, Springer, US, Boston MA, 2015 doi: 10.1007/978-1-4419-8264-3.
[60] D.H. Pearson, C.C. Ahn, B. Fultz, White lines and d -electron occupancies for the 3 d and 4 d transition metals, Phys. Rev. B 47 (1993) 8471–8478, https://doi.org/10.1103/PhysRevB.47.8471.
[61] A. Marucco, Effects of composition on the order-disorder transformation in Ni-Cr based alloys, Key Eng. Mater. 48 (1991) 77–90, https://doi.org/10.4028/www.scientific.net/KEM.48.77.
[62] R.J. Taunt, B. Ralph, Ordering and the K-effect in Ni2Cr, Phys. Status Solidi (A) 29 (1975) 431–442, https://doi.org/10.1002/pssa.2210290211.
[63] T. De Cock, C. Capdevila, F.G. Caballero, C.G. de Andrés, Interpretation of a dilatometric anomaly previous to the ferrite-to-austenite transformation in a low carbon steel, Scr. Mater. 54 (2006) 949–954, https://doi.org/10.1016/j.scriptamat.2005.10.052.
[64] X. Chen, F. Yuan, H. Zhou, X. Wu, Structure motif of chemical short-range order in a medium-entropy alloy, Mater. Res. Lett. 10 (2022) 149–155, https://doi.org/10.1080/21663831.2022.2029607.
[65] X. Chen, Q. Wang, Z. Cheng, M. Zhu, H. Zhou, P. Jiang, L. Zhou, Q. Xue, F. Yuan, J. Zhu, X. Wu, E. Ma, Direct observation of chemical short-range order in a medium-entropy alloy, Nature 592 (2021) 712–716, https://doi.org/10.1038/s41586-021-03428-z.
[66] M. Zhang, Q. Yu, C. Frey, F. Walsh, M.I. Payne, P. Kumar, D. Liu, T.M. Pollock, M. D. Asta, R.O. Ritchie, A.M. Minor, Determination of peak ordering in the CrCoNi medium-entropy alloy via nanoindentation, Acta Mater. 241 (2022) 118380, https://doi.org/10.1016/j.actamat.2022.118380.
[67] F. Walsh, M. Zhang, R.O. Ritchie, A.M. Minor, M. Asta, Extra electron reflections in concentrated alloys may originate from planar defects, not short-range order, ArXiv (2022). http://arxiv.org/abs/2210.01277.
[68] L. Li, Z. Chen, S. Kuroiwa, M. Ito, K. Kishida, H. Inui, E.P. George, Tensile and compressive plastic deformation behavior of medium-entropy Cr-Co-Ni single crystals from cryogenic to elevated temperatures, Int. J. Plast 148 (2022) 103144, https://doi.org/10.1016/j.ijplas.2021.103144.
[69] R.C. Reed, The Superalloys, 1st ed.,, Cambridge University Press, Cambridge UK, 2006 doi: 10.1017/CBO9780511541285.
[70] F. Walsh, M. Asta, R.O. Ritchie, Magnetically driven short-range order can explain anomalous measurements in CrCoNi, Proc. Natl. Acad. Sci. USA 118 (2021) 1–6, https://doi.org/10.1073/pnas.2020540118.
[71] C. Niu, A.J. Zaddach, A.A. Oni, X. Sang, J.W. Hurt, J.M. LeBeau, C.C. Koch, D. L. Irving, Spin-driven ordering of Cr in the equiatomic high entropy alloy NiFeCrCo, Appl. Phys. Lett. 106 (2015) 161906, https://doi.org/10.1063/1.4918996.
[72] M.S. Lucas, G.B. Wilks, L. Mauger, J.A. Muñoz, O.N. Senkov, E. Michel, J. Horwath, S.L. Semiatin, M.B. Stone, D.L. Abernathy, E. Karapetrova, Absence of long-range chemical ordering in equimolar FeCoCrNi, Appl. Phys. Lett. 100 (2012) 251907, https://doi.org/10.1063/1.4730327.